Cell Reports
Medicine

Article

Patient-derived models of brain metastases recapitulate human disseminated disease

Graphical abstract

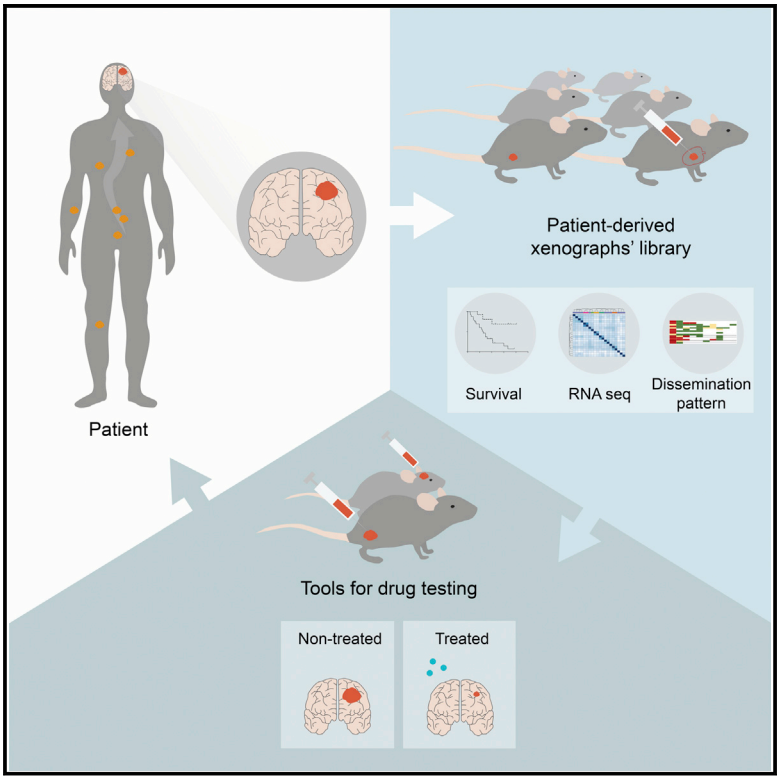

Authors

Claudia C. Faria, Rita Cascão, Carlos Custódia, ..., José Miguéns, Isidro Cortes-Ciriano, João T. Barata

Correspondence

claudiafaria@medicina.ulisboa.pt

In brief

Faria et al. establish a collection of patient-derived xenografts (PDXs) from brain metastases of multiple cancers that resemble the disseminated disease of the patients. Multiple PDXs are tested in preclinical trials for anticancer therapies. Human brain metastases and their matched PDXs have similar gene expression profiles.

Highlights

- Established PDXs of brain metastasis from multiple cancers
- PDXs recapitulate the dissemination pattern of patient tumors
- Patient-derived models of brain metastases are valuable to test anticancer drugs
- Human brain metastases and their PDXs retain similar transcriptional profiles

Faria et al., 2022, Cell Reports Medicine *3*, 100623
May 17, 2022
https://doi.org/10.1016/j.xcrm.2022.100623

CellPress

Cell Reports Medicine

CellPress
OPEN ACCESS

Article

Patient-derived models of brain metastases recapitulate human disseminated disease

Claudia C. Faria,[1,2,5,7,*] Rita Cascão,[1,5] Carlos Custódia,[1,6] Eunice Paisana,[1,6] Tânia Carvalho,[1] Pedro Pereira,[3] Rafael Roque,[3] José Pimentel,[3] José Miguéns,[2] Isidro Cortes-Ciriano,[4] and João T. Barata[1]

[1]Instituto de Medicina Molecular João Lobo Antunes, Faculdade de Medicina, Universidade de Lisboa, Lisboa, Portugal
[2]Department of Neurosurgery, Hospital de Santa Maria, Centro Hospitalar Universitário Lisboa Norte (CHULN), Lisboa, Portugal
[3]Laboratory of Neuropathology, Neurology Department, Hospital de Santa Maria, Centro Hospitalar Universitário Lisboa Norte (CHULN), Lisboa, Portugal
[4]European Molecular Biology Laboratory, European Bioinformatics Institute, Hinxton, Cambridge CB10 1SD, UK
[5]These authors contributed equally
[6]These authors contributed equally
[7]Lead contact
*Correspondence: claudiafaria@medicina.ulisboa.pt
https://doi.org/10.1016/j.xcrm.2022.100623

SUMMARY

Dissemination of cancer cells from primary tumors to the brain occurs in many cancer patients, increasing morbidity and death. There is an unmet medical need to develop translational platforms to evaluate therapeutic responses. Toward this goal, we established a library of 23 patient-derived xenografts (PDXs) of brain metastases (BMs) from eight distinct primary tumors. *In vivo* tumor formation correlates with patients' poor survival. Mouse subcutaneous xenografts develop spontaneous metastases and intracardiac PDXs increase dissemination to the CNS, both models mimicking the dissemination pattern of the donor patient. We test the FDA-approved drugs buparlisib (pan-PI3K inhibitor) and everolimus (mTOR inhibitor) and show their efficacy in treating our models. Finally, we show by RNA sequencing that human BMs and their matched PDXs have similar transcriptional profiles. Overall, these models of BMs recapitulate the biology of human metastatic disease and can be valuable translational platforms for precision medicine.

INTRODUCTION

Metastases are the main cause of cancer morbidity and mortality. Metastatic cancer cells can arise within the brain parenchyma (~40% of cancer patients)[1,2] or spread to the leptomeninges to coat the brain and the spinal cord (~5%–8% of cancer patients).[3] Both clinical conditions are associated with a dismal outcome with a median survival rate of 4 to 6 weeks for untreated patients and 8 to 16 weeks after standard of care therapies (radiotherapy and chemotherapy).[4,5] The primary tumors with the highest predisposition to develop brain metastases (BMs) include lung (40%–60%), breast (15%–30%), and melanoma (5%–15%). Despite the recent medical advances in the treatment of primary tumors, the incidence of BMs has increased. This augmented incidence is most likely due to improved patient survival and thus time for dissemination, inefficacy of primary tumor therapies in treating BMs,[6,7] lack of available drugs that penetrate the blood-brain barrier (BBB),[8,9] and to the selection of chemoresistant metastatic clones upon treatment with DNA damaging agents.[7,10,11]

Although specific genes have been associated with BMs,[12–14] the biological processes underlying the dissemination of cancer cells into the brain are not fully understood, and there is an unmet medical need for the development of targeted therapies. One of the main caveats in advancing the treatment of BMs is the lack of appropriate biological models to study human disease. Conventional preclinical models of BMs are abundant and well characterized, but they fail to reproduce spontaneous dissemination and are frequently used in treatment-naïve situations, a feature that is not commonly seen in cancer patients.[15–18] Genetic mouse models also fail to recapitulate the heterogeneity of primary human cancers and are limited by complex breeding schemes, incomplete tumor penetrance, and variable tumor onset. The generation of patient-derived xenografts (PDXs), by transplantation of patient tumor samples subcutaneously or orthotopically into immune-deficient mice, emerged as a promising tool to better model human disease.[19] These models recapitulate the main histological and genomic features of the parental tumors at a relatively low passage, increasing the interest in this strategy to study the mechanisms of cancer progression and evaluate the therapeutic efficacy of new drugs.[20–22] The ability of PDXs to maintain the phenotypic and molecular signature of human tumors has been described for different types of primary cancers, namely breast cancer,[23,24] lung cancer,[25,26] colon cancer,[27] pancreatic cancer,[28] melanoma,[29] and ovarian carcinoma.[30] On the contrary, studies describing PDXs of BMs are scarce and mainly focused on the most common cancer types.[25,31,32] A recent multi-institutional study generated PDXs from BMs of different primary origins

A

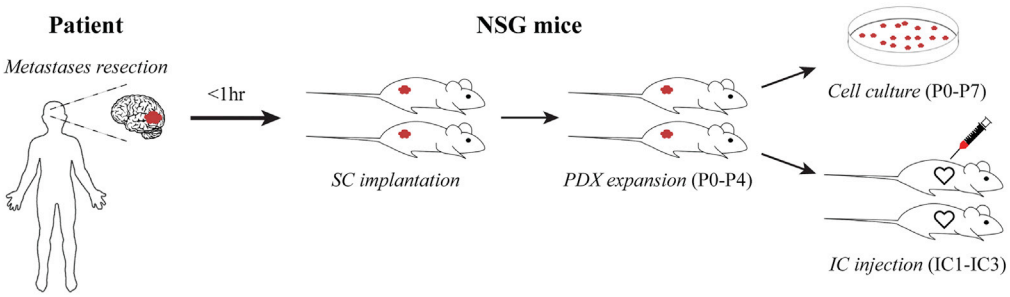

B

Primary tumor	Implanted samples	PDX take rate	Latency time (days)					
			P0	P1	P2	P3	P4	Total
Lung	**17**	**11/17**	66 (33-76)	39 (20-55)	27 (21-45)	33 (24-41)	19 (18-21)	**33 (22-55)**
Colon	**5**	**5/5**	75 (35-111)	43 (27-47)	26 (21-74)	34 (30-47)	31 (28-34)	**37 (27-56)**
Bladder	**2**	**2/2**	73 (70-76)	67	24 (22-26)	35 (31-38)	24	**35 (24-68)**
Melanoma	**1**	**1/1**	30	36	41	50 (40-60)	55 (34-76)	**33 (38-46)**
Osteosarcoma	**1**	**1/1**	27 (21-32)	20	26 (22-29)	18 (14-21)	28 (24-31)	**22 (20-30)**
Endometrium	**1**	**1/1**	57 (32-82)	48 (33-63)	31 (24-38)	33	29	**33 (29-44)**
Prostate	**1**	**1/1**	147 (108-185)	68 (59-77)	---			**93 (64-166)**
Breast	**4**	**1/4**	65 (58-72)	---				**65 (58-72)**
Renal	**2**	**0/2**						
Nasosinusal	**1**	**0/1**						
Total	**35**	**23/35 (66%)**	**65 (32-78)**	**39 (25-61)**	**26 (22-41)**	**33 (25-40)**	**24 (20-30)**	**34 (24-58)**

C

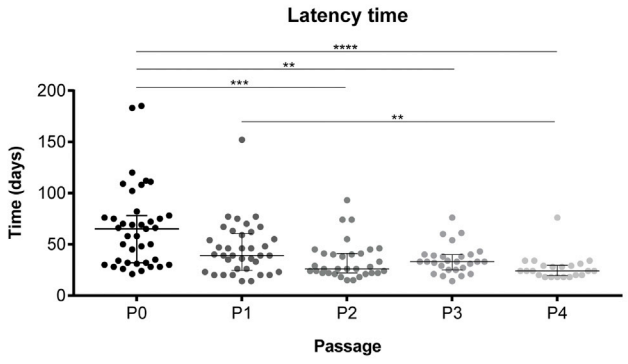

D

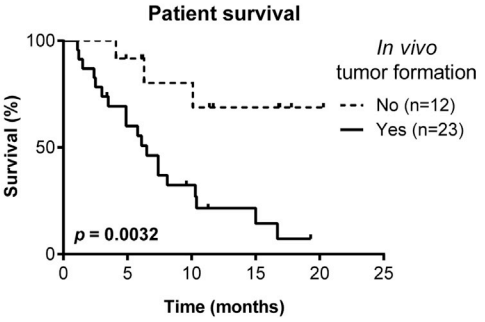

Figure 1. Subcutaneous xenografts derived from BM surgical samples

(A) Experimental workflow for patient-derived models. Samples were implanted in the flank of immuno-compromised NSG mice and serially expanded until passage four. Flank tumors were dissociated into single cell suspensions that were used to establish PDCs up to passage seven, or to perform intracardiac injection in the left cardiac ventricle of NSG mice (up to three serial injections).

(B) Take rate and latency time of subcutaneously implanted human BMs from diverse primary cancers.

(legend continued on next page)

but the potential to use those models as platforms for drug screening was not explored.[33]

Taking advantage of the privileged access to BM samples of patients with detailed clinical annotation, we have developed a library of 35 PDXs of BMs from eight distinct primary tumor origins. We have generated subcutaneous and intracardiac models, performed a histopathological characterization of the tumors, and thoroughly evaluated the pattern of cancer cell dissemination with particular emphasis in the CNS. Also, we have established patient-derived cultures (PDCs) and characterized their pattern of growth and dissemination in orthotopic xenografts. To further validate our patient-derived models of BMs as a tool for precision medicine, we demonstrated the efficacy of Food and Drug Administration (FDA)-approved drugs (the PI3K inhibitor, buparlisib, and the mTOR inhibitor, everolimus) in treating PDCs and the correspondent mouse xenografts using both subcutaneous and orthotopic models. Finally, we have compared the transcriptomic signature of matched patient and mice xenografts by RNA sequencing analysis. Our study demonstrates that PDXs of BMs with a spontaneous metastatic phenotype that recapitulate human disease can effectively be used to preclinically evaluate the response to targeted anticancer therapies. We believe our patient-derived models of BMs constitute a clinically relevant platform for drug discovery and a powerful tool for personalized medicine.

RESULTS

Patient-derived tumor models reflect the clinical spectrum of human brain metastatic disease

Thirty-five surgical specimens were consecutively collected from patients with BMs from 10 different primary cancers (Figure 1 and Table S1), in the Department of Neurosurgery at Hospital de Santa Maria - Centro Hospitalar Universitário Lisboa Norte (CHULN, Lisbon, Portugal). Representation of different primary tumor types in our BM patient cohort reflects the neurosurgical series from our Department of Neurosurgery, having a higher proportion of BMs derived from lung cancer patients. Tumor fragments from each specimen were implanted in the flank of NSG mice within 1 h after surgery. Subcutaneous tumors were serially passaged *in vivo* until passage four. In parallel, cancer cells were dissociated from subcutaneous tumors to generate PDCs of BMs and intracardiac PDXs upon injection of cancer cells into the heart (left ventricle) of mice (Figure 1A). Upon reaching the humane endpoint, animals were euthanized, and all organs were collected for histopathological analysis and to evaluate the presence of metastases. PDCs were successfully generated from 61% (14 of 23) of the engrafted tumors (Table S1).

The cohort of patients that generated the BM tumor models had a median age of 64 years (25–81 years) (Figure S1A), with a male predominance (n = 22; 63%) (Figure S1B). The most common primary cancers were lung (48.5%), colon (14%), and breast cancer (11%) (Figure S1C), reflecting the human tumor types with highest predisposition to originate BMs. Most BMs were located in the supratentorial compartment, in the frontal or temporal lobes (Figures S1D and S1E). Although all primary cancer types disseminated to the supratentorial compartment, only a few were found in the posterior fossa (Figures S1F and S1G). The patients' median survival after the diagnosis of BMs was 6.5 months (Figure S1H) and a trend toward a worse outcome was seen in patients with BMs in the infratentorial compartment (Figure S1I).

In vivo tumorigenicity and clinical aggressiveness of subcutaneously implanted human BMs

Among multiple BMs from 10 different primary cancer origins implanted in the flank of NSG mice, we successfully grew tumors from eight distinct histological types. *In vivo* tumorigenicity was defined as tumor formation within 6 months after flank implantation, confirmed by histopathological analysis. The overall take rate for establishing PDXs of BMs was 66% (Figure 1B). Latency time, defined as the time between subcutaneous implantation of the tumor fragment and the first tumor growth, decreased through passaging (Figure 1C). Notably, the ability of transplants to form tumors *in vivo* correlated with the donor patient's clinical outcome, demonstrating the potential prognostic value of these models. BMs with tumor formation capacity *in vivo* (n = 23) derived from patients with an overall survival of 6.1 months, in contrast with BMs unable to engraft in mice (n = 12) whose patients had an overall survival of 10.8 months (Figure 1D; $p = 0.0032$). These differences were also observed in patients with lung cancer BMs (Figure S2A; $p = 0.0286$). The *in vivo* tumorigenic potential was associated with older age (Figure S2B) and higher number of extracranial metastatic sites (Figure S2C). Local treatment of BMs (Figure S2D) and systemic therapy to the primary tumor (Figure S2E) with radiation therapy seemed to decrease the engraftment ability in mice. Patient gender and tumor location were not associated with tumor engraftment (Figures S2F–S2H).

Spontaneous dissemination of cancer cells in subcutaneous xenografts

To elucidate the metastatic potential of the implanted human BMs, we performed histopathological analysis of all the organs in each mouse. These subcutaneous xenografts have some advantages compared with the orthotopic models, avoiding the artificial implantation of cancer cells in the brain without the possibility to assess systemic dissemination, and preventing the disruption of the BBB. Remarkably, of the 23 tumors engrafted in the flank of NSG mice, 61% (n = 14) originated spontaneous metastases to different sites, suggesting that cancer cells derived from BMs maintain their original metastatic potential. Moreover, we observed homing of cancer cells to the primary tumor site in 78% (7 of 9) of lung cancer BMs (Figure 2A and Figures S3A–S3D). The sites of metastases across serial *in vivo* passaging varied with different human samples and occurred

(C) Tumor latency time decreases upon *in vivo* serial passaging (n = 2 NSG mice/passage for each engrafted BM sample).
(D) The *in vivo* tumorigenic potential of BM surgical samples correlates with patient poor survival. Data are expressed as median with interquartile range. Differences were considered statistically significant for p values <0.05, according to the Kruskal-Wallis with Dunn's multiple comparisons and Log rank (Mantel-Cox) tests. See also Table S1, Figures S1 and S2.

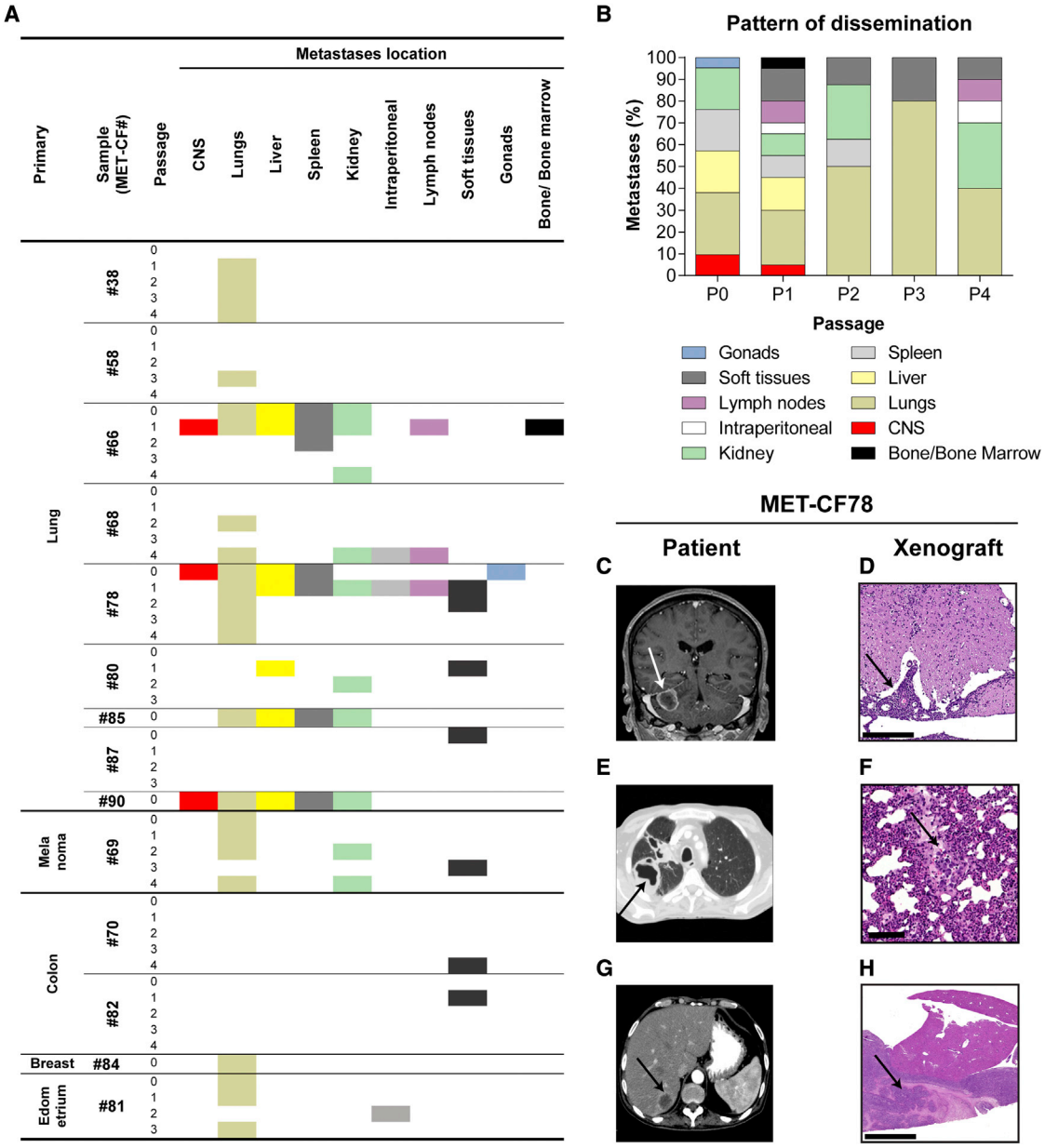

Figure 2. Spontaneous dissemination of subcutaneously implanted tumors

(A) Systemic location of metastases observed in mice subcutaneously implanted with human BMs throughout passages (n = 2 NSG mice/passage for each engrafted BM sample).

(B) Pattern of dissemination of cancer cells across *in vivo* passages (n = 50).

(C–H) Representative clinical case of a 61-year-old male patient (MET-CF78) with metastatic lung carcinoma to the brain and to the liver, whose PDX mimicked the donor patient disease. (C) Magnetic resonance imaging of the brain, coronal T1 contrast-enhanced, showing a right cerebellar hemisphere metastasis. (D) H&E staining of the mouse lumbar spinal cord with leptomeningeal dissemination (arrow). (E) Computed tomography (CT) scan of the patient's thorax showing a primary lung cancer on the right lung and (F) H&E staining of the matched mouse lung with a metastasis (arrow). (G) Patient abdominal CT scan showing a liver metastasis (arrow) and (H) the matched liver metastasis in the xenograft. Scale bars, (D) 250 μm, (F) 100 μm, (H) 1 mm. See also Figures S3 and S4 and Table S2.

both at early and late passages. Interestingly, the spontaneous metastatic phenotype to the CNS (3 of 14; 21%) was observed in early passages and presented as leptomeningeal dissemination. The number of metastatic sites decreased with *in vivo* passaging (Figure 2B), possibly due to loss of heterogeneity from selection of more proliferative clones.

We have compared the pattern of dissemination of each PDX with the patient from whom the sample derived. We found that the pattern of spontaneous cancer dissemination in some subcutaneous PDXs recapitulated the metastatic phenotype of the patients' disease (Table S2). Mouse xenografts and matched patients mirrored the metastatic sites in seven samples (50%). For

A

Primary tumor	No. of samples	Survival time (days)			
		IC1	IC2	IC3	Total
Lung	6	167 (126-259)	77 (39-114)	63 (10-69)	**88 (59-160)**
Colon	3	93 (79-186)	88 (77-199)	72 (71-89)	**83 (72-101)**
Bladder	1	45	67 (56-77)	38	**45 (42-67)**
Melanoma	1	114	75 (68-75)	61 (58-63)	**75 (63-114)**
Osteosarcoma	1	64	66 (58-79)	-	**64 (61-72)**
Endometrium	1	163 (153-173)	131	76	**131 (76-163)**
Total	**13**	**114 (67-175)**	**77 (66-110)**	**71 (60-75)**	**77 (64-114)**

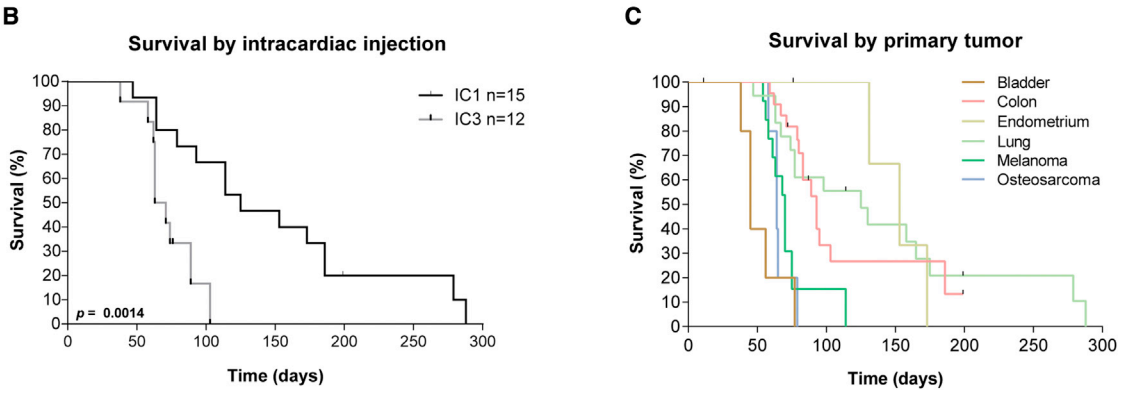

Figure 3. Intracardiac xenografts derived from human BM samples

(A) Survival of mice submitted to intracardiac injections of cancer cells derived from human BMs of diverse primary tumors. Data are expressed as median with interquartile range.

(B) Kaplan-Meier of mice survival curves in early (IC1) and late (IC3) intracardiac xenograft passages.

(C) Mice overall survival according to the primary tumor (n = 76). Differences were considered statistically significant for p values <0.05, according to the Log rank (Mantel-Cox) test.

example, the PDX derived from MET-CF78 exhibited metastatic deposits in the same organs as the patient with stage IV lung cancer from where it was originated (Figures 2C–2H). MET-CF69 was derived from a patient with metastatic melanoma and diffuse lung infiltration, a pattern also observed in the corresponding xenograft (Figure S3E–S3H). Three lung cancer BMs from patients with parenchymal disease gave origin to animal models with spontaneous leptomeningeal dissemination to the CNS (21%) (Figures 2C, 2D and S4).

Intracardiac PDXs increase the metastatic potential of cancer cells to the CNS and mimic human disease

The injection of cancer cells in the left cardiac ventricle of mice has been previously validated as a good animal model for the study of BMs. We have generated PDCs from 14 BMs grown in the flank of mouse xenografts (subcutaneous PDXs), which were consecutively passaged by intracardiac injection (up to passage 3) into NSG mice (Figure 3A). The most common primary tumors were lung cancer (40%) and colon cancer (27%). Mouse survival decreased with passaging (Figures 3A and 3B), likely reflecting the selection of more aggressive clones, and varied according to the primary tumor type (Figure 3C). Interestingly, intracardiac PDXs derived from infratentorial metastases showed a trend toward a worse outcome, similar to the BMs patient cohort (Figure S1I).

All the intracardiac PDXs analyzed developed systemic metastases. As expected from the delivery of cancer cells into the blood stream, the number of metastatic sites increased when compared with subcutaneous tumor implantation (Figure 4A). The intracardiac model also increased the tropism of cancer cells to the CNS (6 of 13; 46%), either focal metastases in the parenchyma (4 of 6) or leptomeningeal dissemination (2 of 6), particularly at later passages (Figure 4B).

When we compared the pattern of cancer cell dissemination in the intracardiac xenograft models with the respective patient staging of metastatic disease (Table S3), we observed that eight

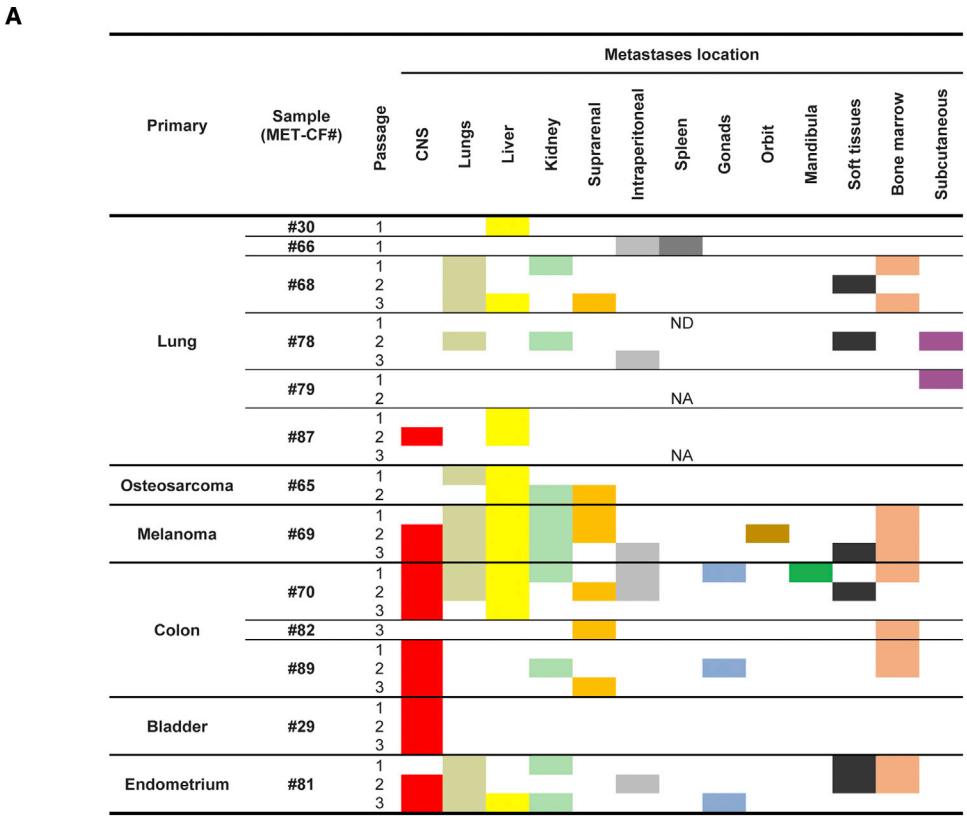

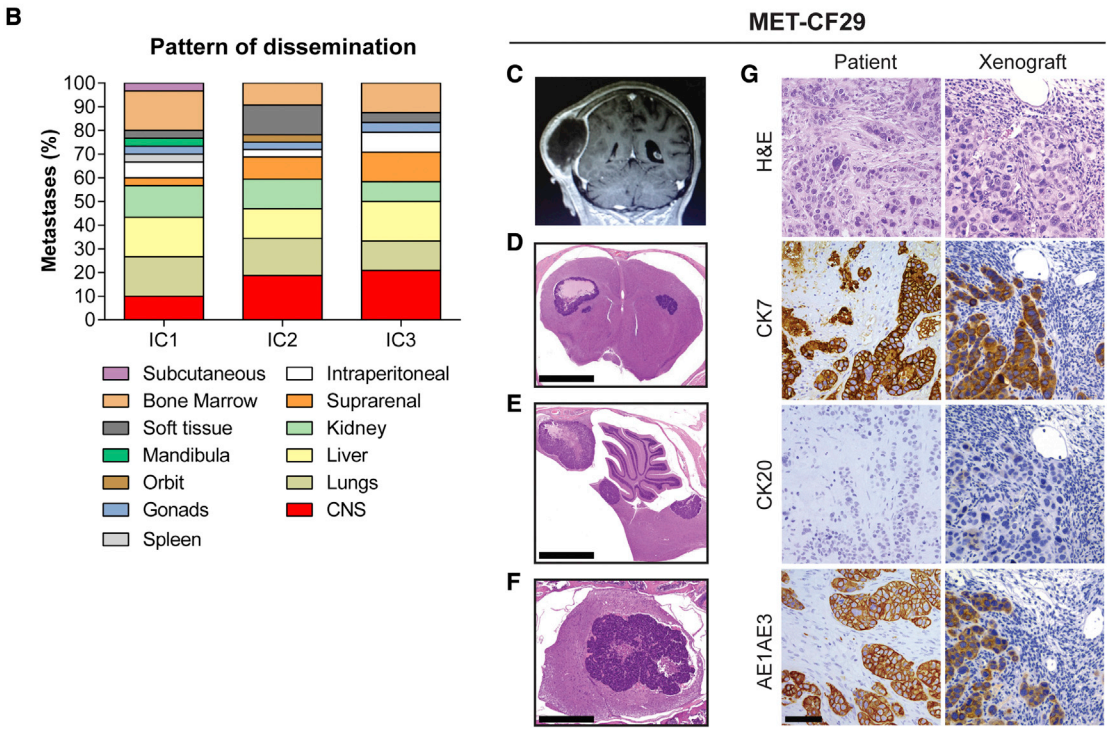

(legend on next page)

PDXs (62%) recapitulated the donor metastatic sites and three PDXs (23%) mirrored the intracranial location of the patient's tumor (Figure S5). Of notice, MET-CF29-derived PDX originated from a patient with metastatic bladder carcinoma, exhibited metastases exclusive to the CNS and the same pattern of immunostaining as the corresponding patients' BM (Figures 4C–4G).

Altogether, our results demonstrate that intracardiac PDXs of BMs recapitulate human metastatic disease and may constitute good models to study CNS dissemination from diverse primary cancers.

In vitro therapeutic response of PDCs to targeted anticancer drugs

The lack of appropriate models of BMs that reproduce the biology of patients' disease, limited their use as platforms to assess drug efficacy *in vitro* and *in vivo*. We have established PDCs from different primary cancers in order to validate their utility as *in vitro* models for drug testing. We selected two FDA-approved drugs, buparlisib (pan-PI3K inhibitor) and everolimus (mTOR inhibitor), already in use in the clinic, targeting two pathways relevant in metastatic cancer, and previously tested in orthotopic preclinical models of breast cancer BMs.[32] We have evaluated the effect of these compounds in PDCs from four different types of primary tumors: MET-CF69 (melanoma-derived BM), MET-CF78 (lung cancer-derived BM), MET-CF81 (endometrium cancer-derived BM), and MET-CF89 (colon cancer-derived BM), as shown in Figure 5. *In vitro* treatment with two different concentrations of buparlisib (1 and 10 μM) and everolimus (20 nM and 1 μM) induced variable responses regarding pathway inhibition and cell proliferation. Buparlisib effectively inhibited pAkt in all PDCs, while everolimus inhibited the downstream target pS6, mainly in MET-CF81 and MET-CF89 (Figures 5A, 5D, 5G, and 5J). The effect in cell proliferation was higher for buparlisib, inhibiting proliferation in all PDCs (Figures 5B, 5E, 5H, and 5K). Everolimus was effective inhibiting proliferation in two PDCs from lung cancer and endometrium cancer, but it only reached statistical significance in lung cancer-derived cells (Figures 5C, 5F, 5I, and 5L).

Effective therapeutic response of PDXs to targeted anticancer drugs

To assess the potential of our PDXs in evaluating the response to targeted therapies, we tested *in vivo* the same drugs, which have already demonstrated efficacy in orthotopic mouse models of BMs from breast cancer.[32] As shown above, both compounds effectively inhibited their expected targets at low concentrations in our PDCs. Importantly, buparlisib and everolimus cross the BBB, which is crucial in treating brain tumors. First, we tested these compounds in a subcutaneous xenograft model using MET-CF78 cells (from a lung cancer BM) (Figure 6A). Mice were treated with three cycles of oral therapy with buparlisib or everolimus. Both compounds effectively reduced tumor growth (Figure 6B) and tumor size by the end of the treatment protocol (Figures 6C, 6D, and 6E).

We have also generated orthotopic xenograft models upon intracranial injection of two PDCs from lung cancer (MET-CF78) and melanoma (MET-CF69) (Figure S6). In these aggressive models of BMs, median mice survival is of approximately 1 to 1.5 months (Figures S6A, S6B, S6D and S6E) and cancer cells show a highly invasive phenotype in the brain parenchyma (Figures S6C, S6F and S6G). In addition, the lung cancer model can disseminate within the CNS. Mice harboring MET-CF78 intracranial tumors were treated with three cycles of oral therapy with buparlisib or everolimus (Figure 6F). Both compounds were effective in reducing brain tumor size (Figure 6G) and everolimus was also effective in decreasing brain leptomeningeal dissemination (Figure 6H). No differences were found in spinal cord dissemination between untreated controls and treated mice (Figure 6I). We repeated the experimental approach with an intracranial melanoma PDX (MET-CF69) (Figure S7A) and observed an effective reduction in brain tumor size (Figure S7D). In both models, no variations in the body weight of mice were observed, as a measure of compound-induced toxicity (Figures S7B and S7C).

These observations are a proof-of-concept that our patient-derived models provide a useful tool for preclinical testing of anticancer therapies.

Human BMs and their matched xenografts have similar gene expression profiles

To determine whether our patient-derived models recapitulate the original patient BMs, at the transcriptional level, we have performed RNA sequencing of patient BMs from diverse primary tumors (lung cancer, colon cancer, prostate cancer, endometrium cancer, and melanoma) and their matched subcutaneous PDX tumors. Paired human BMs and their corresponding PDX tumors have similar transcriptional profiles and cluster together in a principal component analysis (PCA), confirming that these models resemble human disease (Figures 7A and 7B).

DISCUSSION

PDX models have recently emerged as good preclinical platforms for drug discovery in oncology.[18,21,29] The development of PDXs from BMs has been focused on the most common cancer types. Contreras-Zarate et al. successfully generated PDXs of breast cancer BMs upon implantation in the mammary fat

Figure 4. Metastatic phenotype in intracardiac xenograft models of human BMs

(A) Systemic location of metastases observed in mice after intracardiac injection of human BMs throughout passages (n = 2 NSG mice/passage for each engrafted BM sample, passages IC1–IC3).

(B) Pattern of dissemination of cancer cells across *in vivo* intracardiac injections (n = 48).

(C–G) Intracardiac mouse xenograft from a 70-year-old female patient with a bladder carcinoma (MET-CF29). (C) Contrast-enhanced coronal T1 magnetic resonance image sequence of a parietal skull metastasis with adjacent dural and subcutaneous tissue invasion. Representative H&E-stained sections of the correspondent mouse xenograft revealing exclusive CNS metastases, (D) in the supratentorial compartment, (E) in the infratentorial compartment, and (F) in the spinal cord. (G) Comparison of the immunohistochemical markers for bladder carcinoma between human BM sample and corresponding xenografted tumor. Scale bars, (D) 1 mm, (E) 1 mm, (F) 250 μm, (G) 50 μm. See also Figure S5 and Table S3.

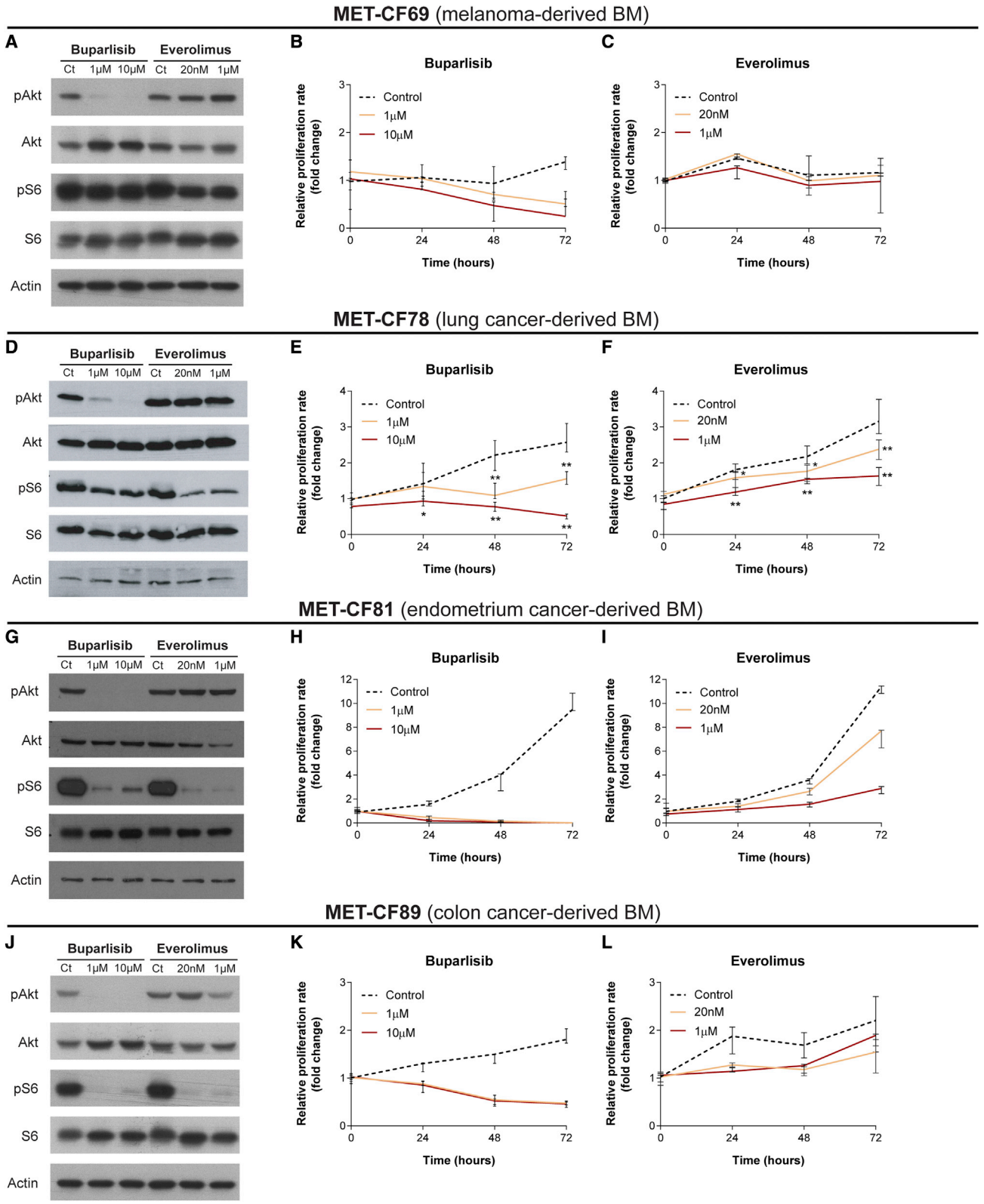

(legend on next page)

pad.[31] Lee et al. established subcutaneous and orthotopic PDXs from non-small cell lung cancer primary tumors and BMs, which maintained the histopathological similarities and the molecular profiling signatures of the parental tumors. The intracardiac injection of primary cultured human cancer cells in mice originated systemic tumors but failed to recapitulate the metastatic phenotype of the patients' disease.[25] Another study described spontaneous metastases in melanoma subcutaneous PDXs but no correspondence with patients' disease was reported.[29] A multi-omic characterization comparing PDXs of central nervous system metastases and the original patient tumors showed maintained molecular profiles.[33] However, the authors did not explore the utility of these models for preclinical testing of anticancer therapies. Our study describes patient-derived models of BMs, with spontaneous dissemination to different organs, recapitulating the patients' disease. Moreover, we demonstrate that these models can be used to assess the efficacy of anticancer compounds.

We took the advantage of having privileged access to tumor tissue from human BMs to develop a pipeline of patient-derived models from multiple cancers (Figure 7C). A collection of 23 well-established PDXs of BMs from eight distinct primary cancers was developed, phenotypically characterized over time, and compared with the original patients' metastatic disease. We systematically generated subcutaneous PDXs, intracardiac PDXs, intracranial PDXs, and PDCs to comprehensively assess the ability of these models to engraft and to disseminate. Each model has its advantages and limitations. Subcutaneous PDX models are easier to establish and to monitor drug efficacy through measurement of tumor volume, and to evaluate spontaneous dissemination to different organs. However, they exhibit low incidence of spontaneous dissemination, particularly to the CNS. Intracardiac PDXs exhibit higher incidence of BMs, which can be explained due to the injection of cancer cells in the arterial blood stream. In our models, we observed a high incidence of spontaneous metastases (100%), increased CNS dissemination (46%), and a higher number of metastatic sites shared between xenografts and donor patients (62%), which confirms that these models better represent the patients' disease. Intracranial PDXs of BMs take into consideration the microenvironment of human BMs and allow the assessment of the BBB crossing by small molecule compounds.

Despite these advantages, the described models have important limitations. Similar to BM in cancer patients, spontaneous BMs occur late in subcutaneous PDXs, often requiring surgical removal of the flank tumor to prevent premature endpoint due to severe extracranial disease.[34] Furthermore, the incidence of BM is low, which increases variability and the demand for larger cohorts of animals. *In vivo* drug screening in these models is costly and time-consuming, dissociating from the limited survival time of the patients with BM and limiting the possibility to use these PDXs as "avatars" of cancer patients.[35] Intracranial inoculation of cancer cells induces artificial disruption of the BBB and does not recapitulate the metastatic cascade, since cancer cells do not require extravasation. Systemic inoculation of cancer cells from BM induces significant extracranial metastatic burden, which can be problematic to assess survival and to test drug efficacy in brain metastatic disease.[34] An alternative would be to inject cancer cells into the carotid artery, but this procedure is more invasive, technically more complex, and, therefore, not as readily applicable as intracardiac inoculation. Moreover, this model misses the early steps of the metastatic cascade, including invasion and the formation of a premetastatic niche. Finally, in all the above-mentioned PDX models, cancer cells from BMs are implanted in mice without the primary tumor, which does not resemble the clinical scenario.

The library of xenograft-matched PDCs we generated constitutes an excellent tool for testing anticancer compounds. It has been previously shown that orthotopic PDXs of HER2-positive breast cancer BMs could be successfully treated with PI3K and mTOR inhibitors (buparlisib and everolimus, respectively).[36] The combination of these targeted therapies resulted in durable tumor regressions and downstream pathway inhibition.[32] These compounds have the advantage of being in use in clinical trials for several human cancers.[37] We have shown the effect of buparlisib and everolimus in treating PDCs from different primary cancers. Interestingly, the inhibitory effects in downstream signaling and the inhibition in cell proliferation varied according to specific cancer cell types. Finally, we treated subcutaneous and intracranial PDXs with weekly protocols of oral buparlisib and everolimus, showing decrease in tumor size and in leptomeningeal dissemination. Although we tested a limited number of compounds, not taking into consideration possible targeted therapies depending on cancer type, we have shown these models are suitable for preclinical testing of novel compounds or repurposing drugs already in use in the clinic.

The analysis of primary tumors and metastases from different organs and patients has identified a landscape of genomic heterogeneity.[38] The transformation of a local tumor into a systemic tumor is a highly complex multistep process, much more difficult to treat. Recent studies using mouse models of cancer provided evidence of polyclonal seeding of cancer cells, which often disseminate in parallel to form metastases, and of cooperation between subclones to enhance tumor progression.[39–42] Phylogenetic analysis of matched samples from metastatic cancer patients corroborated those findings and demonstrated that metastasis-to-metastasis spread is a common event.[43] These mechanisms likely enhance tumor heterogeneity and may potentially contribute to drug resistance. We have performed RNA sequencing analysis on human BMs and their matched PDXs

Figure 5. PDCs of BMs from diverse primary tumor origins were used to assess the efficacy of PI3K and mTOR inhibitors

(A–L). PDCs were established from surgical BM samples derived from patients with (A)–(C) melanoma, (D)–(F) lung carcinoma, (G)–(I) endometrium cancer, and (J)–(L) colon cancer. (A, D, G, J) Representative western blots demonstrate different patterns of Pi3K and mTOR pathway inhibition after incubation of PDCs with buparlisib and everolimus, respectively. Inhibition of cell proliferation upon treatment with increasing doses of buparlisib (B, E, H, K) and everolimus (C, F, I, L) also show different levels of inhibition among BM-derived PDCs. Cell viability was measured using MTS assay. Data are represented as median with interquartile range, with three technical replicates. Differences were considered statistically significant for p values <0.05, according to the Mann-Whitney test.

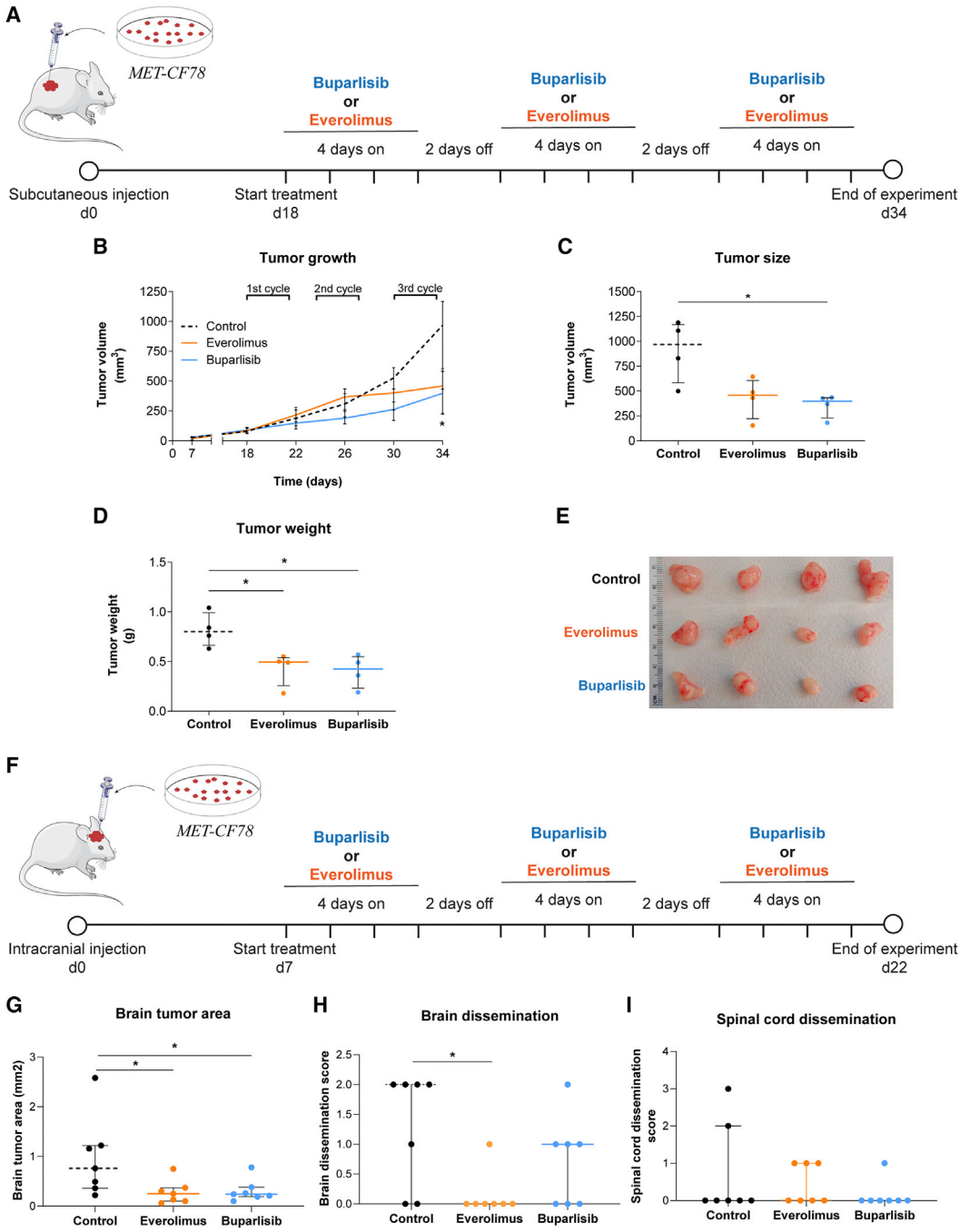

Figure 6. PDXs of a lung cancer BM respond to PI3K and mTOR inhibition

(A) Representative scheme of the treatment protocol performed in a xenograft established after the subcutaneous injection of the PDC derived from a lung cancer BM (MET-CF78). Animals were randomly divided in three groups: buparlisib (30 mg/kg/day; n = 4), everolimus (3 mg/kg/day; n = 4), and vehicle (5% DMSO/30% PEG300/H_2O; n = 4) used as control for comparison.

(B–D) Inhibition of flank tumor growth upon three cycles of therapy with buparlisib and everolimus (B). Significant reduction in (C) tumor size and (D) tumor weight by the end of treatment.

(E) Representative photographs of flank tumors in each experimental group by the end of treatment.

(F–I) Representative scheme of the treatment protocol performed in an orthotopic xenograft established after intracranial injection of the same PDC (F). Animals were randomly divided into three groups: buparlisib (30 mg/kg/day; n = 7), everolimus (3 mg/kg/day; n = 7), and vehicle (5% DMSO/30% PEG300/H_2O; n = 7) used as control for comparison. Treatment administration was also performed in three cycles of therapy with buparlisib and everolimus. Histological sections of the CNS were evaluated to assess the (G) tumor area in the brain as well as (H) brain and (I) spinal cord dissemination. Data are represented as median with interquartile range. Differences were considered statistically significant for p values <0.05, according to the Mann-Whitney test. See also Figures S6 and S7.

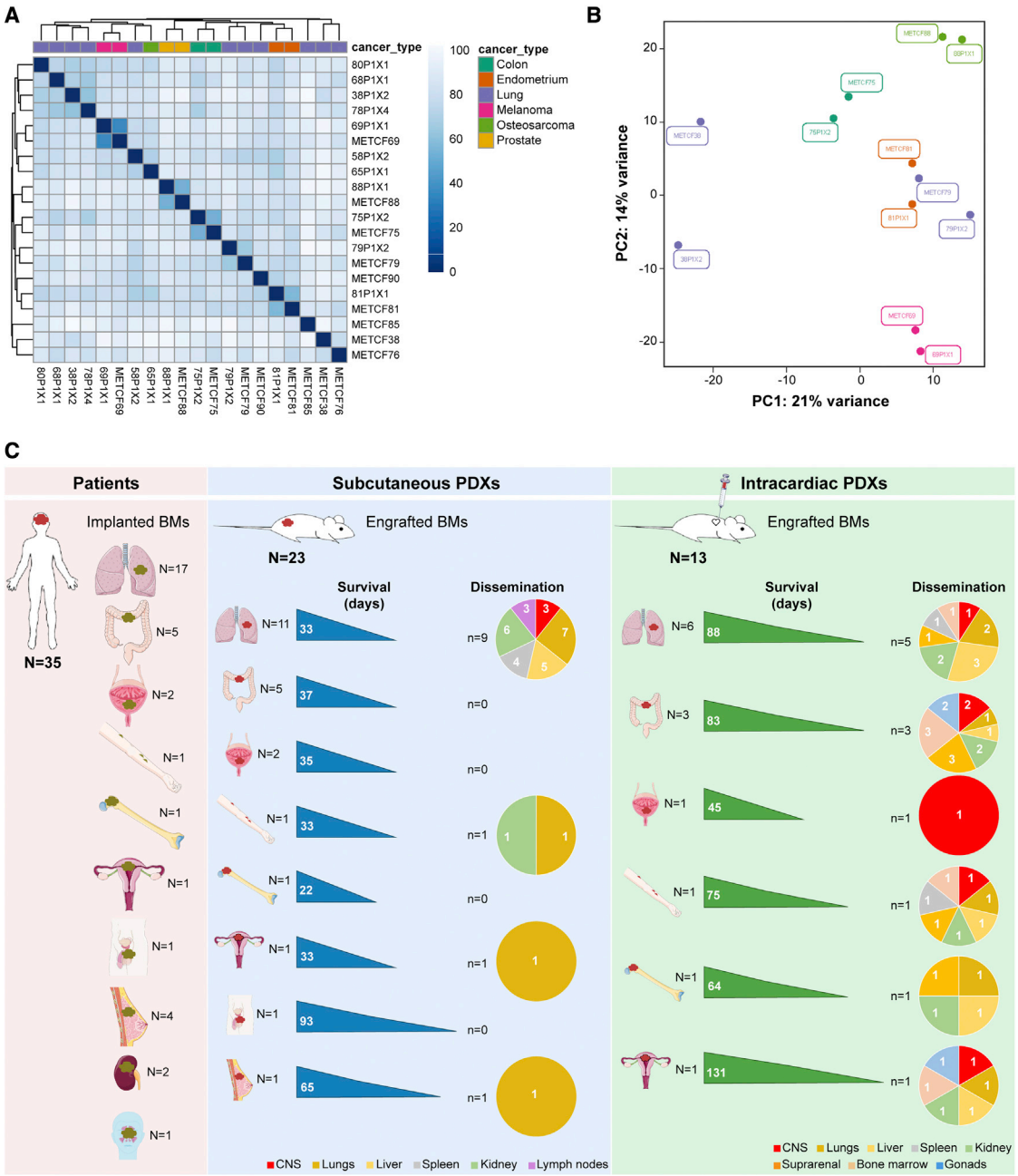

Figure 7. Transcriptional profiling and pattern of dissemination of patient-derived xenografts of BMs

(A and B) RNA sequencing of human BMs (n = 9) from diverse primary tumors and their matched PDXs (n = 11) reveals similar gene expression profiles in the (A) heatmap analysis and in the (B) PCA plot.

(C) Overview of the study design and main findings. Scheme illustrating our cohort of BMs samples from cancer patients with diverse primary tumor origins, and their respective subcutaneous and intracardiac PDXs. This scheme depicts take rates, survival, and dissemination pattern in each established model.

and found that they have similar transcriptional profiles. However, future genomic studies need to confirm the clonal identity of each metastatic site in our PDXs, since the observed pattern of cancer dissemination over serial passaging in mice, particularly with the intracardiac injection, might reflect the conservation of inter- and intra-tumoral heterogeneity. Another limitation of our study is the lack of comparison to the primary tumors, regarding the transcriptomic profile and the response to anticancer drugs.

The translational models reported in this study (using BMs of diverse primary cancer origins that recapitulate the dynamics of cancer cell dissemination, mirror patient metastatic disease, and respond to anticancer therapies) represent an outstanding

tool to the scientific community in advancing our understanding of the mechanisms of tumor spread and fostering the rapid discovery and repurposing of novel therapeutics.

Limitations of the study

A limitation of this study includes the resources, the time, and the associated costs needed to develop the various PDX models of BM. Each model has specific limitations related to the site of implantation of cancer cells, limiting the possibility to study all the steps of the metastatic cascade. Subcutaneous PDXs have low incidence of BM due to the premature endpoint imposed by the rapid growth of the flank tumor, increasing variability and demanding a large sample size. Intracardiac PDXs induce extensive extracranial metastatic burden preventing the use of survival to assess drug efficacy in BM. Intracranial models artificially disrupt the BBB, bypassing the extravasation step of the metastatic cascade. Further preclinical studies are needed to assess the efficacy of combined anticancer therapies. Although paired BM and subcutaneous PDXs have similar gene expression profiles, future genomic studies are important to investigate the clonal identity of each metastatic site in our PDXs.

STAR★METHODS

Detailed methods are provided in the online version of this paper and include the following:

- KEY RESOURCES TABLE
- RESOURCE AVAILABILITY
  - Lead contact
  - Materials availability
  - Data and code availability
- EXPERIMENTAL MODEL AND SUBJECT DETAILS
  - Ethics approval and consent to participate
  - Human BM samples
  - Sample nomenclature
  - Patient-derived xenografts from BMs
  - Patient-derived cultures from BMs
- METHOD DETAILS
  - Subcutaneous PDXs
  - Intracardiac PDXs
  - Orthotopic PDXs
  - Histological and immunohistochemical analysis
  - Cell viability
  - Western blotting
  - *In vivo* drug treatment using subcutaneous PDXs
  - *In vivo* drug treatment using orthotopic PDX
  - mRNA sequencing
- QUANTIFICATION AND STATISTICAL ANALYSIS

SUPPLEMENTAL INFORMATION

Supplemental information can be found online at https://doi.org/10.1016/j.xcrm.2022.100623.

ACKNOWLEDGMENTS

The authors acknowledge the patients who kindly provided the tumor specimens used to generate the PDX models needed for this research. The Biobanco-iMM CAML enabled the process of tumor specimen collection, processing, and storage. Finally, the authors acknowledge the Histology and Comparative Pathology Laboratory from Instituto de Medicina Molecular João Lobo Antunes for technical assistance. C.C. was supported by a fellowship from Fundação para a Ciência e a Tecnologia (FCT, SFRH/BD/140299/2018). E.P. was supported by a fellowship from FCT (PD/BD/128288/2017). This project was funded by FCT (PTDC/MED-ONC/32222/2017), Fundação Millennium bcp, and by private donations. This work was also supported by UID/BIM/50005/2019 and co-funded by FCT/Ministério da Ciência, Tecnologia e Ensino Superior (MCTES) through funds of Programa de Investimento e Despesas de Desenvolvimento da Administração Central (PIDDAC). The funders had no role in study design, data collection and analysis, decision to publish, or preparation of the manuscript.

AUTHOR CONTRIBUTIONS

Study design, C.C.F., R.C., and J.T.B.; study conduct, R.C., C.C., E.P., T.C., P.P., and R.R.; data collection, C.C.F., R.C., C.C., E.P., T.C., P.P., and R.R.; data analysis, C.C.F., R.C., C.C., E.P., T.C., and I.C.-C.; data interpretation, C.C.F., R.C., C.C., E.P., T.C., I.C.-C., and J.T.B.; drafting manuscript, C.C.F. and R.C.; revising manuscript content, C.C.F., R.C., C.C., E.P., T.C., P.P., R.R., J.P., J.M., I.C.-C., and J.T.B.; approving final version of manuscript, C.C.F., R.C., C.C., E.P., T.C., P.P., R.R., J.P., J.M., I.C.-C., and J.T.B.; C.C.F., R.C., C.C., E.P., T.C., P.P., R.R., J.P., J.M., I.C.-C., and J.T.B. take responsibility for the integrity of the data analysis.

DECLARATION OF INTERESTS

The authors declare no competing interests.

Received: June 17, 2021
Revised: February 1, 2022
Accepted: April 8, 2022
Published: May 3, 2022

REFERENCES

1. Gavrilovic, I.T., and Posner, J.B. (2005). Brain metastases: epidemiology and pathophysiology. J. Neurooncol. *75*, 5–14.
2. Achrol, A.S., Rennert, R.C., Anders, C., Soffietti, R., Ahluwalia, M.S., Nayak, L., Peters, S., Arvold, N.D., Harsh, G.R., Steeg, P.S., et al. (2019). Brain metastases. Nat. Rev. Dis. Primers *5*, 5.
3. Taillibert, S., and Chamberlain, M.C. (2018). Leptomeningeal metastasis. Handb. Clin. Neurol. *149*, 169–204.
4. Leal, T., Chang, J.E., Mehta, M., and Robins, H.I. (2011). Leptomeningeal metastasis: challenges in diagnosis and treatment. Curr. Cancer Ther. Rev. *7*, 319–327.
5. Soffietti, R., Ahluwalia, M., Lin, N., and Ruda, R. (2020). Management of brain metastases according to molecular subtypes. Nat. Rev. Neurol. *16*, 557–574.
6. Lin, N.U., Bellon, J.R., and Winer, E.P. (2004). CNS metastases in breast cancer. J. Clin. Oncol. *22*, 3608–3617.
7. Lin, X., and DeAngelis, L.M. (2015). Treatment of brain metastases. J. Clin. Oncol. *33*, 3475–3484.
8. Groves, M.D. (2010). New strategies in the management of leptomeningeal metastases. Arch. Neurol. *67*, 305–312.
9. Lockman, P.R., Mittapalli, R.K., Taskar, K.S., Rudraraju, V., Gril, B., Bohn, K.A., Adkins, C.E., Roberts, A., Thorsheim, H.R., Gaasch, J.A., et al. (2010). Heterogeneous blood-tumor barrier permeability determines drug efficacy in experimental brain metastases of breast cancer. Clin. Cancer Res. *16*, 5664–5678.
10. Heerboth, S., Housman, G., Leary, M., Longacre, M., Byler, S., Lapinska, K., Willbanks, A., and Sarkar, S. (2015). EMT and tumor metastasis. Clin. Transl. Med. *4*, 6.

11. Venur, V.A., Chukwueke, U.N., and Lee, E.Q. (2020). Advances in management of brain and leptomeningeal metastases. Curr. Neurol. Neurosci. Rep. *20*, 26.

12. Bos, P.D., Zhang, X.H., Nadal, C., Shu, W., Gomis, R.R., Nguyen, D.X., Minn, A.J., van de Vijver, M.J., Gerald, W.L., Foekens, J.A., et al. (2009). Genes that mediate breast cancer metastasis to the brain. Nature *459*, 1005–1009.

13. Brastianos, P.K., Carter, S.L., Santagata, S., Cahill, D.P., Taylor-Weiner, A., Jones, R.T., Van Allen, E.M., Lawrence, M.S., Horowitz, P.M., Cibulskis, K., et al. (2015). Genomic characterization of brain metastases reveals branched evolution and potential therapeutic targets. Cancer Discov. *5*, 1164–1177.

14. Valiente, M., Obenauf, A.C., Jin, X., Chen, Q., Zhang, X.H., Lee, D.J., Chaft, J.E., Kris, M.G., Huse, J.T., Brogi, E., et al. (2014). Serpins promote cancer cell survival and vascular co-option in brain metastasis. Cell *156*, 1002–1016.

15. Tentler, J.J., Tan, A.C., Weekes, C.D., Jimeno, A., Leong, S., Pitts, T.M., Arcaroli, J.J., Messersmith, W.A., and Eckhardt, S.G. (2012). Patient-derived tumour xenografts as models for oncology drug development. Nat. Rev. Clin. Oncol. *9*, 338–350.

16. Rosfjord, E., Lucas, J., Li, G., and Gerber, H.P. (2014). Advances in patient-derived tumor xenografts: from target identification to predicting clinical response rates in oncology. Biochem. Pharmacol. *91*, 135–143.

17. Hidalgo, M., Amant, F., Biankin, A.V., Budinska, E., Byrne, A.T., Caldas, C., Clarke, R.B., de Jong, S., Jonkers, J., Maelandsmo, G.M., et al. (2014). Patient-derived xenograft models: an emerging platform for translational cancer research. Cancer Discov. *4*, 998–1013.

18. Masmudi-Martin, M., Zhu, L., Sanchez-Navarro, M., Priego, N., Casanova-Acebes, M., Ruiz-Rodado, V., Giralt, E., and Valiente, M. (2021). Brain metastasis models: what should we aim to achieve better treatments? Adv. Drug Deliv. Rev. *169*, 79–99.

19. Lai, Y., Wei, X., Lin, S., Qin, L., Cheng, L., and Li, P. (2017). Current status and perspectives of patient-derived xenograft models in cancer research. J. Hematol. Oncol. *10*, 106.

20. Siolas, D., and Hannon, G.J. (2013). Patient-derived tumor xenografts: transforming clinical samples into mouse models. Cancer Res. *73*, 5315–5319.

21. Bruna, A., Rueda, O.M., Greenwood, W., Batra, A.S., Callari, M., Batra, R.N., Pogrebniak, K., Sandoval, J., Cassidy, J.W., Tufegdzic-Vidakovic, A., et al. (2016). A biobank of breast cancer explants with preserved intra-tumor heterogeneity to screen anticancer compounds. Cell *167*, 260–274.e22.

22. Rubio-Viqueira, B., Jimeno, A., Cusatis, G., Zhang, X., Iacobuzio-Donahue, C., Karikari, C., Shi, C., Danenberg, K., Danenberg, P.V., Kuramochi, H., et al. (2006). An in vivo platform for translational drug development in pancreatic cancer. Clin. Cancer Res. *12*, 4652–4661.

23. Charafe-Jauffret, E., Ginestier, C., Bertucci, F., Cabaud, O., Wicinski, J., Finetti, P., Josselin, E., Adelaide, J., Nguyen, T.T., Monville, F., et al. (2013). ALDH1-positive cancer stem cells predict engraftment of primary breast tumors and are governed by a common stem cell program. Cancer Res. *73*, 7290–7300.

24. Li, S., Shen, D., Shao, J., Crowder, R., Liu, W., Prat, A., He, X., Liu, S., Hoog, J., Lu, C., et al. (2013). Endocrine-therapy-resistant ESR1 variants revealed by genomic characterization of breast-cancer-derived xenografts. Cell Rep. *4*, 1116–1130.

25. Lee, H.W., Lee, J.I., Lee, S.J., Cho, H.J., Song, H.J., Jeong, D.E., Seo, Y.J., Shin, S., Joung, J.G., Kwon, Y.J., et al. (2015). Patient-derived xenografts from non-small cell lung cancer brain metastases are valuable translational platforms for the development of personalized targeted therapy. Clin. Cancer Res. *21*, 1172–1182.

26. Dong, X., Guan, J., English, J.C., Flint, J., Yee, J., Evans, K., Murray, N., Macaulay, C., Ng, R.T., Gout, P.W., et al. (2010). Patient-derived first generation xenografts of non-small cell lung cancers: promising tools for predicting drug responses for personalized chemotherapy. Clin. Cancer Res. *16*, 1442–1451.

27. Metildi, C.A., Kaushal, S., Luiken, G.A., Talamini, M.A., Hoffman, R.M., and Bouvet, M. (2014). Fluorescently labeled chimeric anti-CEA antibody improves detection and resection of human colon cancer in a patient-derived orthotopic xenograft (PDOX) nude mouse model. J. Surg. Oncol. *109*, 451–458.

28. Nicolle, R., Blum, Y., Marisa, L., Loncle, C., Gayet, O., Moutardier, V., Turrini, O., Giovannini, M., Bian, B., Bigonnet, M., et al. (2017). Pancreatic adenocarcinoma therapeutic targets revealed by tumor-stroma cross-talk analyses in patient-derived xenografts. Cell Rep. *21*, 2458–2470.

29. Krepler, C., Sproesser, K., Brafford, P., Beqiri, M., Garman, B., Xiao, M., Shannan, B., Watters, A., Perego, M., Zhang, G., et al. (2017). A comprehensive patient-derived xenograft collection representing the heterogeneity of melanoma. Cell Rep. *21*, 1953–1967.

30. Ricci, F., Bizzaro, F., Cesca, M., Guffanti, F., Ganzinelli, M., Decio, A., Ghilardi, C., Perego, P., Fruscio, R., Buda, A., et al. (2014). Patient-derived ovarian tumor xenografts recapitulate human clinicopathology and genetic alterations. Cancer Res. *74*, 6980–6990.

31. Contreras-Zarate, M.J., Ormond, D.R., Gillen, A.E., Hanna, C., Day, N.L., Serkova, N.J., Jacobsen, B.M., Edgerton, S.M., Thor, A.D., Borges, V.F., et al. (2017). Development of novel patient-derived xenografts from breast cancer brain metastases. Front. Oncol. *7*, 252.

32. Ni, J., Ramkissoon, S.H., Xie, S., Goel, S., Stover, D.G., Guo, H., Luu, V., Marco, E., Ramkissoon, L.A., Kang, Y.J., et al. (2016). Combination inhibition of PI3K and mTORC1 yields durable remissions in mice bearing orthotopic patient-derived xenografts of HER2-positive breast cancer brain metastases. Nat. Med. *22*, 723–726.

33. Tew, B.Y., Legendre, C., Schroeder, M.A., Triche, T., Gooden, G.C., Huang, Y., Butry, L., Ma, D.J., Johnson, K., Martinez, R.A., et al. (2020). Patient-derived xenografts of central nervous system metastasis reveal expansion of aggressive minor clones. Neuro Oncol. *22*, 70–83.

34. Schwartz, H., Blacher, E., Amer, M., Livneh, N., Abramovitz, L., Klein, A., Ben-Shushan, D., Soffer, S., Blazquez, R., Barrantes-Freer, A., et al. (2016). Incipient melanoma brain metastases instigate astrogliosis and neuroinflammation. Cancer Res. *76*, 4359–4371.

35. Miarka, L., and Valiente, M. (2021). Animal models of brain metastasis. Neurooncol. Adv. *3*, v144–v156.

36. Blazquez, R., Wlochowitz, D., Wolff, A., Seitz, S., Wachter, A., Perera-Bel, J., Bleckmann, A., Beissbarth, T., Salinas, G., Riemenschneider, M.J., et al. (2018). PI3K: a master regulator of brain metastasis-promoting macrophages/microglia. Glia *66*, 2438–2455.

37. LoRusso, P.M. (2016). Inhibition of the PI3K/AKT/mTOR pathway in solid tumors. J. Clin. Oncol. *34*, 3803–3815.

38. Hu, Z., Li, Z., Ma, Z., and Curtis, C. (2020). Multi-cancer analysis of clonality and the timing of systemic spread in paired primary tumors and metastases. Nat. Genet. *52*, 701–708.

39. McFadden, D.G., Papagiannakopoulos, T., Taylor-Weiner, A., Stewart, C., Carter, S.L., Cibulskis, K., Bhutkar, A., McKenna, A., Dooley, A., Vernon, A., et al. (2014). Genetic and clonal dissection of murine small cell lung carcinoma progression by genome sequencing. Cell *156*, 1298–1311.

40. Cleary, A.S., Leonard, T.L., Gestl, S.A., and Gunther, E.J. (2014). Tumour cell heterogeneity maintained by cooperating subclones in Wnt-driven mammary cancers. Nature *508*, 113–117.

41. Sanborn, J.Z., Chung, J., Purdom, E., Wang, N.J., Kakavand, H., Wilmott, J.S., Butler, T., Thompson, J.F., Mann, G.J., Haydu, L.E., et al. (2015). Phylogenetic analyses of melanoma reveal complex patterns of metastatic dissemination. Proc. Natl. Acad. Sci. U S A *112*, 10995–11000.

42. Marjanovic, N.D., Hofree, M., Chan, J.E., Canner, D., Wu, K., Trakala, M., Hartmann, G.G., Smith, O.C., Kim, J.Y., Evans, K.V., et al. (2020). Emergence of a high-plasticity cell state during lung cancer evolution. Cancer Cell *38*, 229–246.e13.

43. Gundem, G., Van Loo, P., Kremeyer, B., Alexandrov, L.B., Tubio, J.M.C., Papaemmanuil, E., Brewer, D.S., Kallio, H.M.L., Hognas, G., Annala, M., et al. (2015). The evolutionary history of lethal metastatic prostate cancer. Nature *520*, 353–357.

44. Dankner, M., Caron, M., Al-Saadi, T., Yu, W., Ouellet, V., Ezzeddine, R., Maritan, S.M., Annis, M.G., Le, P.U., Nadaf, J., et al. (2021). Invasive growth associated with cold-inducible RNA-binding protein expression drives recurrence of surgically resected brain metastases. Neuro Oncol. *23*, 1470–1480.

45. Dobin, A., Davis, C.A., Schlesinger, F., Drenkow, J., Zaleski, C., Jha, S., Batut, P., Chaisson, M., and Gingeras, T.R. (2013). STAR: ultrafast universal RNA-seq aligner. Bioinformatics *29*, 15–21.

46. Anders, S., Pyl, P.T., and Huber, W. (2015). HTSeq–a Python framework to work with high-throughput sequencing data. Bioinformatics *31*, 166–169.

47. Love, M.I., Huber, W., and Anders, S. (2014). Moderated estimation of fold change and dispersion for RNA-seq data with DESeq2. Genome Biol. *15*, 550.

STAR★METHODS

KEY RESOURCES TABLE

REAGENT or RESOURCE	SOURCE	IDENTIFIER
Antibodies		
Mouse Anti-human Cytokeratin 7	Thermo Fisher Scientific	180234; RRID:AB_86727
Mouse Anti-human Cytokeratin 20	Agilent	M7019; RRID:AB_2133718
Mouse Cytokeratin Pan antibody Cocktail (AE1AE3)	Thermo Fisher Scientific	MA5-13203, RRID:AB_10942225
Phospho-Akt (Ser473) (D9E) XP® Rabbit mAb	Cell Signaling Technology	Cat#4060, RRID: AB_231504
Akt Antibody	Cell Signaling Technology	Cat#9272, RRID:AB_329827
Phospho-S6 Ribosomal Protein (Ser235/236) Antibody	Cell Signaling Technology	Cat#2211, RRID:AB_331679
S6 Ribosomal Protein (5G10) Rabbit mAb	Cell Signaling Technology	Cat#2217, RRID:AB_331355
Anti-β-Actin Antibody (C4)	Santa Cruz	sc-47778, RRID:AB_2714189
Anti-Rabbit IgG (H+L), HRP Conjugate	Promega	W4011
Anti-Mouse IgG (H+L), HRP Conjugate	Promega	W4021
Biological samples		
35 Brain Metastases collected from patients	This study	N/A
PDX samples	This study	N/A
PDCs	This study	N/A
Chemicals, peptides, and recombinant proteins		
Buparlisib (NVP-BKM120)	Selleckchem	S2247
Everolimus (RAD001)	Selleckchem	S1120
B-27™ Supplement (50X), serum free	Gibco™	17504044
DMEM/F-12	Gibco™	11320074
HEPES (1 M)	Gibco™	15630080
L-Glutamine (200 mM)	Gibco™	A2916801
rhEGF	Merck Life Science	E9644
Human Recombinant bFGF	StemCell Technologies	78003
N-2 Supplement (100X)	Gibco™	17502048
Kynurenic Acid	Sigma-Aldrich	K3375
Trypsin from porcine pancreas	Sigma-Aldrich	T4799
Deoxyribonuclease I from bovine pancreas	Sigma-Aldrich	DN25
Hyaluronidase from sheep testes	Sigma-Aldrich	H6254
Trypsin inhibitor from chicken egg white	Sigma-Aldrich	T9253
Matrigel® Matrix	Corning®	354324
Poly(ethylene glycol) average Mn 300	Sigma-Aldrich	202371-500G
Dimethyl sulfoxide (DMSO)	Sigma-Aldrich	D2650
Laminin from Engelbreth-Holm-Swarm murine sarcoma basement membrane	Sigma-Aldrich	L-2020
Poly-L-ornithine solution	Sigma-Aldrich	P4957
Accutase® solution	Sigma-Aldrich	A6964
Trizma-Base	Sigma-Aldrich	93362
Sodium Cloride (NaCl)	Sigma-Aldrich	S3014
Ethylenediaminetetraacetic acid (EDTA)	Sigma-Aldrich	E6758
Fetal Bovine Serum	Biowest	S181B-500
Euthasol: Sodium Pentobarbital 400mg/ml	Dechra	N/A
Isovet: Isoflurane 1000mg/g 250ml	B. Braun Medical	N/A
Bupaq: Buprenorphine 0,3mg/ml	Plurivet	N/A

(*Continued on next page*)

Continued

REAGENT or RESOURCE	SOURCE	IDENTIFIER
Critical commercial assays		
CellTiter 96® Aqueous One Solution Cell Proliferation Assay (MTS)	Promega	G3580
6.5 mm Transwell® with 8.0 μm Pore Polyester Membrane Insert	Corning	3464
PhosSTOP™	Roche	4906845001
cOmplete™, Mini Protease Inhibitor Cocktail	Roche	11836153001
Nitrocellulose Membrane 0.2 μm	Bio-Rad	1620112
Bio-Rad Protein Assay Dye Reagent Concentrate	Bio-Rad	5000006
Pierce™ ECL Western Blotting Substrate	ThermoFisher Scientific	32106
EnVision+/HRP, Rabbit, HRP. Rabbit	Agilent	K4003
Deposited data		
RNAseq of human brain metastases	Sequence Read Archive (SRA)	BioProject: PRJNA820633
Experimental models: Cell lines		
MET-CF78	This Study	N/A
MET-CF89	This Study	N/A
MET-CF70	This Study	N/A
MET-CF69	This Study	N/A
MET-CF29	This Study	N/A
MET-CF81	This Study	N/A
Experimental models: Organisms/strains		
NOD.Cg-PrkdcscidIl2rgtm1Wjl/SzJ	Charles River Laboratories	RRID: IMSR_JAX:005557
Software and algorithms		
FIJI	Schindelin J, et al. 2012	https://fiji.sc/
GraphPad Prism version 8.0.0 for Windows	GraphPad Software	https://www.graphpad.com/
G*Power 3.1 software	Heinrich-Heine University of Dusseldorf	http://www.gpower.hhu.de
RANDOM.ORG: True Random Number Service.	Randomness and Integrity Services Ltd.	https://www.random.org
STAR 2.7.4a	Dobin et al, 2013	https://github.com/alexdobin/STAR
HTSeq (v.0.6.1p1)	Anders et al, 2014	https://htseq.readthedocs.io/en/master/index.html
DESeq2	Love et al, 2014	https://bioconductor.org/packages/release/bioc/html/DESeq2.html
Other		
Novosyn - Mid-term absorbable braided and coated suture made of polyglactin 910	Braun	G0068213
Medical X-Ray Film Blue	Agfa	CP-BU New
Corning® Primaria™ 100 mm x 20 mm Standard Cell Culture Dish	Corning	353803
Falcon™ Cell Strainers 70μm	Fisher Scientific	352350
Epredia™ Lab Vision™ PT Module	Fisher Scientific	A80400012

RESOURCE AVAILABILITY

Lead contact

Further information and resource requests should be directed to and will be fulfilled by the lead contact, Claudia C. Faria (claudiafaria@medicina.ulisboa.pt).

Materials availability

PDXs and PDCs generated in this study are available from the lead contact with a completed materials transfer agreement.

Data and code availability

- Original western blot images and microscopy data reported in this paper will be shared by the lead contact upon request.
- Sequencing data generated in this study have been deposited at the Sequence Read Archive (SRA) under accession number PRJNA820633 and are publicly available as of the date of publication.
- Any additional information required to reanalyze the data reported in this paper is available from the lead contact upon request.

EXPERIMENTAL MODEL AND SUBJECT DETAILS

Ethics approval and consent to participate

Human samples used in this study were collected and stored at Biobanco-iMM CAML (Biobank of the Lisbon Academic Medical Center, Lisbon, Portugal) in accordance with the Centro Hospitalar Universitário Lisboa Norte Ethics Board (Ref[a]. Nº 367/18 and Ref[a]. Nº 346/20). A written informed consent was obtained from all patients prior to study participation.

Experiments involving the use of mice were carried out in accordance with Directive 2010/63/EU (transposed to Portuguese legislation through Decreto-Lei No. 113/2013, of August 7th), and all animal procedures were approved by the institutional animal welfare body (ORBEA-iMM) and licensed by the Portuguese competent authority (license number: 012,028\2016).

Human BM samples

BM samples were resected during surgery from 35 patients with diverse types of tumors (see Table S1 and Figure S1 for patient characterization) at the Department of Neurosurgery from Hospital de Santa Maria, from 2015 to 2017. Surgical BM samples, not needed for diagnostic purposes, were divided into four portions within 1 h after surgery and used for: subcutaneous implantation into NOD.Cg-Prkdcscid Il2rgtm1Wjl/SzJ (NSG) mice, RNA extraction, histological assessment, and storage (see Figure 1A). All samples were included in our brain tumor collection and requested from Biobanco-iMM CAML.

Sample nomenclature

Each sample ID follows the structure MET-CFAA-BC, where:

AA: number of the sample
B: named as P for subcutaneous xenografts and IC for intracardiac xenografts
C: number of the subcutaneous passage or intracardiac round of injection

Patient-derived xenografts from BMs

All animal studies were approved by the institutional animal welfare body (ORBEA-iMM) and conducted in accordance with Directive 2010/63/EU (transposed to Portuguese legislation through Decreto-Lei No. 113/2013, of August 7th) to ensure that the use of animals complies with all applicable legislation and following the 3R's principle. The project was also licensed by the Portuguese competent authority (Direcção Geral Animal e Veterinária; license number: 012028\2016). All animals were kept in specific pathogen-free (SPF) conditions, randomly housed per groups under standard laboratory conditions (at 20-22°C under 10-h light/14-h dark), and given free access to food (RM3, SDS Diets, Witham, UK) and water (Ultrapure).

For this study, NSG mice (males and females) were used to establish *in vivo* models of patient-derived BMs: subcutaneous, intracardiac and orthotopic (intracranial) xenografts. Animals were purchased from Charles River Laboratories (Massachusetts, USA) or obtained from an NSG colony established in-house. Humane endpoints were established for all patient-derived xenografts (PDXs), including: 10% body weight loss, head-tilt, neurological disorders (such as paralysis and stereotypic behavior), or abdominal distension. Additionally, model-specific humane endpoints were applied: subcutaneous PDXs - 1000mm^3 tumor volume; intracranial PDXs - tumor outgrowth palpable in the skull. All surgical procedures were performed under volatile anesthesia (Isoflurane; B. Braun Medical) and mice were given 100μL of 15 μg/mL buprenorphine (Plurivet), monitored for any signals of distress (such as cardiorespiratory arrest), and allowed to recover on a heating pad. Animals were monitored at least once a week. Once they reached the humane endpoint, animals were euthanized by intraperitoneal injection of 140 mg/kg sodium pentobarbital (Euthasol). Unless otherwise stated, CNS, femur and tibia, liver, lungs, spleen, pancreas, adrenal and reproductive systems, lymph nodes, and kidneys were collected during necropsy of all animals and H&E histopathologic analysis was performed blindly by a pathologist.

In this study we used both male and female NSG mice to establish our PDXs, independently of patient gender (exceptions made for breast, prostate, and endometrium cancers). However, no comparison between male and female animals was performed regarding sample engraftment and dissemination, due to low number of animals per passage (n = 2) derived from our in-house colony and respecting the 3Rs principle. Treatment studies with everolimus and buparlisib were performed exclusively in female mice, as in previous publications.

Patient-derived cultures from BMs

Freshly harvested subcutaneous PDX tumors were minced using sterile scalpel blades and enzymatically dissociated using 4 μg/mL trypsin, 2 μg/mL hyaluronidase, 500 ng/mL kynurenic acid, DNase (Sigma-Aldrich) in DMEM/F12 (Gibco), at 37°C with agitation for

~30min. After digestion, 10mL of DMEM/F12 containing 700ng of trypsin inhibitor (Sigma-Aldrich) were added to the suspension and incubated for 5 min at 37°C with agitation. The resulting cell suspensions were filtered through a 70μm cell strainer (Fisher Scientific) and then centrifuged at 1000rpm for 5min. Supernatants were discarded, and pelleted cells were washed in DMEM/F12. Dissociated cells were cultured in DMEM/F12 supplemented with 2% B-27 supplement, 1% HEPES, 1% L-Glutamine, 1x Antibiotic-Antimycotic (Gibco), 0.02 μg/mL rhbFGF (StemCell Technologies) and 0.02 μg/mL rhEGF (Merck LifeScience), and seeded in poly-L-ornithine and Laminin (Sigma-Aldrich) coated dishes (Corning) at 37°C with 5% CO_2. Growth factors were supplemented every $^2/_3$ days. Upon 80% confluency, cells were dissociated using Accutase solution (Sigma-Aldrich) and reseeded onto new coated culture dishes.

METHOD DETAILS

Subcutaneous PDXs

To generate PDXs of human BMs, we subcutaneously implanted a small fragment (4 × 4 × 4mm) of the BM biopsy in 10–20 weeks old NSG mice (1 fragment per mouse; n = 2 mice/sample/passage), not previously used in other experiments. Animals were sutured with absorbable suture line (Novosyn), with no more than 2 stitches. Once palpable, tumor size was measured twice a week using a caliper, and the volume was estimated using the formula $(AxB^2)/2$ where A is the length and B is the width measurement. Upon reaching the humane endpoint, subcutaneous tumors were collected and serially passaged *in vivo* by surgical implantation of a small tumor fragment (4 × 4 × 4mm) in the subcutaneous area. Tumors were serially passaged until passage (P) 4 (see Figure 1A). The remaining tissue was collected for histopathological analysis, cryopreserved in FBS (Biowest) with 10% DMSO (Sigma-Aldrich) and stored in liquid nitrogen. Whenever there was enough tissue available, tumors were also dissociated into single cell suspension and used in the generation of intracardiac PDXs and patient-derived cultures. A total of 280 mice, both males and females, were used to generate these subcutaneous PDXs. Mice were gender matched with patients for prostate (male), breast (female), and endometrial tumors (female).

Intracardiac PDXs

To further understand the metastatic potential of cancer cells, subcutaneous tumors obtained during necropsy were used to generate intracardiac models, as mentioned above. A portion of the tumor was dissociated into single cell suspensions (using the same method as described above for PDCs) and 50000 viable cells (counted using trypan blue exclusion) re-suspended in 80μL PBS were injected in the left ventricle of 10–20 weeks old NSG mice (both males and females; n = 2 mice/sample/injection), not previously used in other experiments. A total of 76 animals were used to generate these intracardiac PDXs. Mice were gender matched with patients only for the BMs of endometrial tumor (female).

Orthotopic PDXs

To understand the growth pattern of cancer cells in the brain, we generated orthotopic PDXs of BMs by the intracranial injection of 100000 viable PDCs (MET-CF 69 and 78). Cells were re-suspended in 3μL of PBS and injected in the brain frontal region (bregma as reference, x = 2mm, y = 0mm z = −2mm) of 10–20 weeks NSG mice (male or females; n = 3 mice/sample), not previously used in other experiments. Upon necropsy only the CNS was collected. A total of 7 mice were used to generate these orthotopic PDX models.

Histological and immunohistochemical analysis

All histological human samples from BM patients were obtained in collaboration with the Laboratory of Neuropathology (Neurology Department, Hospital de Santa Maria, Centro Hospitalar Universitário Lisboa Norte (CHULN), Lisboa, Portugal).

Tissue samples from our mouse PDXs were obtained at necropsy and fixed immediately in 10% neutral buffered formalin solution. Samples containing bone were further decalcified in 10% formic acid. All samples were processed for paraffin embedding. For morphological examination, serial 3μm sections were stained with hematoxylin and eosin (H&E) and immunohistochemistry (IHC) was performed using the following antibodies: mouse anti-human Cytokeratin 7 (Thermo Fisher Scientific), mouse anti-human Cytokeratin 20 (Agilent), mouse Cytokeratin Pan antibody Cocktail (AE1AE3; Thermo Fisher Scientific). The tissue sections were pre-treated in a Epredia™ Lab Vision™ PT Module (Fisher Scientific) at low-Ph, followed by incubation with the primary antibodies. EnVision Link horseradish peroxidase/DAB visualization system (Agilent) was used, and sections were then counterstained with hematoxylin and mounted. Histopathological analysis of H&E and IHC slides was performed blindly by 2 pathologists, and representative photomicrographs were taken using Leica DM2500 brightfield microscope coupled to a Leica MC170 HD microscope camera, or NanoZoomer SQ system (acquisition at 20x digital magnification).

To better understand both cell growth and invasion patterns of PDCs in the CNS, we analyzed H&E-stained brain and spinal cord tissue sections from orthotopic PDXs. Tumors were classified using a semi-quantitative score to evaluate tumor dimensions: 0 – no tumor; 1 – minimal to mild; 2 – moderate; and 3 – marked. Leptomeningeal dissemination was assessed using 2 semi-quantitative scoring systems: distribution score – 0: no tumor; 1: multifocal, minimal-mild; 2: multifocal moderate; and 3: diffuse dissemination; and a cell density score – 0: no cells; 1: minimal to mild; 2: moderate; and 3: marked cellular density. Invasion pattern was evaluated using an adaptation of the scoring system developed by Dankner *et al*.[44] Minimally invasive (MI) tumors scored with 0 or 1 (0 – lesion surrounded by lymphocytes; 1 – defined BM margin with brain parenchyma) and highly invasive (HI) tumors scored with 2 or 3 (2 – defined BM margin with small pockets of invading cells in the parenchyma, but close to the border; and 3 – extensive single-cells invasion or big cell clusters invading the surrounding parenchyma).

Cell viability

To assess the impact of buparlisib and everolimus in cell proliferation, we have used the CellTiter 96 Aqueous One Solution Reagent (MTS; Promega). PDCs were seeded in coated 96-well plates, 1000 cells per well, and incubated up to 72h with either 1μM or 10μM buparlisib (PI3K inhibitor, Selleckchem), and with either 20nM or 1μM of everolimus (mTOR inhibitor, Selleckchem). Cells were then incubated for 2h with MTS and the absorbance was measured at 490nm using Microplate Reader TECAN Infinite M200. Two independent experiments were performed with 3 technical repetitions each.

Western blotting

For western blot analysis, cells were seeded in 6-well plates at 0.5×10^6 cells per well and incubated for 2h with the aforementioned drug concentrations. Cell lysates used for immunoblotting were prepared by directly add to plated cells a lysis buffer (50mM Trizma-Base; 150mM NaCl; 5mM EDTA; Sigma-Aldrich) supplemented with 1x PhosStop phosphatase inhibitors (Roche) and 1x complete™ protease inhibitor cocktail (Roche). After centrifugation at 10000g for 15 min, the supernatant was harvested. Protein concentration was determined using the Bradford protein assay (Protein Assay Dye Reagent Concentrate; BioRad). Equal amounts of protein were used for SDS-PAGE and transferred onto nitrocellulose membranes (BioRad), which were then blocked with 3% skim milk for 1 h at room temperature, incubated with the primary antibodies overnight, and incubated with the appropriate secondary antibodies (anti-rabbit and anti-mouse IgG, HRP Conjugate; Promega) for 1h at room temperature. After incubation, membranes were washed and incubated with Pierce™ ECL Western Blotting Substrate before film (Agfa) exposure. Exposed film was developed using an Agfa Curix 60 automated film processor. Antibodies against p-S473-AKT (1:1000), AKT (1:1000), p-(S235/236)-S6 (1:2000) and S6 (1:2000) (Cell Signaling Technology) and actin (1:1000) (Santa Cruz Biotechnology) were used. Each band was analyzed with a constant frame.

In vivo drug treatment using subcutaneous PDXs

To validate our patient-derived models of BMs as a tool to be used in the *in vivo* test of new drugs, we have assessed the efficacy of FDA approved drugs in treating our subcutaneous PDXs. NSG mice (females, 10-20 weeks old), not previously used for other experiments, were injected subcutaneously in the flank with 100μL of 1:1 mix containing 1.5×10^6 viable PDCs in PBS 1x and Matrigel (Corning). In this experiment, we have used PDCs isolated from the MET-CF78 (lung cancer-derived BM). When all tumors were measurable (tumor size range of 50-150mm^3 by day 18 post injection), animals were randomized (using a random sequence generator; Random.org) into three groups of 4 mice each: vehicle control (N = 4; 5% DMSO +30% PEG300 + H2O; Sigma-Aldrich), buparlisib (N = 4; 30 mg/kg/day; PI3K inhibitor, Sellekchem) and everolimus (N = 4; 3 mg/kg/day; mTOR inhibitor, Selleckchem). Drugs were re-suspended in DMSO and freshly diluted in vehicle solution immediately prior administration, according to the manufacturers' instructions. Mice received three cycles of therapy (four days on and two days off) by oral gavage. Mice were euthanized one day after the final treatment (day 34 post injection). The optimal experimental group size was calculated based on a Power analysis statistical test using the G*Power 3.1 software (http://www.gpower.hhu.de). The test was based on an *a priori* analysis, comparing the medians of the experimental groups using the Mann-Whitney test, with alpha (error probability) = 0.05, power = 0.95 and effect size = 4.0434 and actual power = 0.95 (calculated based on Bruna et al[21]); http://www.polyu.edu.hk/mm/effectsizefaqs/calculator/calculator.html. Thus, the optimal size of the experimental groups was determined to be 3 animals per group. To ensure the power of the experiment, 1 extra animal was added per group. A total of 12 animals were used in this experiment.

In vivo drug treatment using orthotopic PDX

To further validate our patient-derived models of BMs as a tool to be used in the *in vivo* test of new drugs, we have assessed the efficacy of the same compounds in treating our orthotopic PDXs. In this experiment, we have used PDCs from MET-CF78 (lung cancer-derived BM, 5×10^4 cells/mouse) and from MET-CF69 (melanoma-derived BM, 1×10^5 cells/mouse) to inject intracranially in NSG mice (females, 10-20 weeks old, not previously used in other experiments). Animal randomization and treatment cycles were the same as described for the treatment of the subcutaneous PDXs. Treatment of MET-CF78-injected mice started 7 days post-injection, whereas treatment of MET-CF69-injected mice started 19 days post-injection. One day after the last treatment administration, animals were euthanized (see Figure S7). The optimal experimental group size was calculated based on Power analysis statistical test using the G*Power 3.1 software (http://www.gpower.hhu.de). The test was based on an *a priori* analysis, comparing the medians of the experimental groups using the Mann-Whitney test, with alpha (error probability) = 0.05, power = 0.95 and effect size = 2.2766 and actual power = 0.95 (calculated based on our subcutaneous treatment experiment; http://www.polyu.edu.hk/mm/effectsizefaqs/calculator/calculator.html). Thus, the optimal size of the experimental groups was determined to be 6 animals per group. To ensure the power of the experiment, 1 extra animal was added per group. A total of 42 animals were used in these experiments, 7 mice/group for each cell line.

mRNA sequencing

At least 1μg of purified total RNA with RIN ≥5.0 were required. Library preparation was conducted using the Truseq stranded mRNA Library Preparation kit (Illumina). Libraries were sequenced on an Illumina NovaSeq6000 in paired-end mode (2 x 150bp; Macrogen Spain Inc.). Sequencing reads were mapped to the transcriptome using STAR (version 2.7.4a).[45] Gene expression counts were generated using HTSeq (v.0.6.1p1)[46] and normalized to transcripts per kilobase million (TPM). GENCODE v22 was used as the

gene annotation reference. Differential expression analysis was performed using DESeq2[47] using an adjusted p value of 0.01 as the cut-off for statistical significance.

QUANTIFICATION AND STATISTICAL ANALYSIS

Normality distribution was assessed by D'Agostino and Pearson test. Statistical differences were determined with non-parametric Kruskal-Wallis (Dunn's Multiple Comparison tests) and Mann-Whitney tests. Survival curves were analyzed using log rank tests (Mantel-Cox). All statistical analyses were performed using the GraphPad Prism v6.0 (GraphPad, California, USA). Sample size was represented as n. Differences were considered statistically significant for $p < 0.05$. Group size calculation was performed for treatment assays as described in the method details section. Further relevant information can be found on each figure legend.

Cell Reports Medicine, Volume *3*

Supplemental information

Patient-derived models of brain metastases recapitulate human disseminated disease

Claudia C. Faria, Rita Cascão, Carlos Custódia, Eunice Paisana, Tânia Carvalho, Pedro Pereira, Rafael Roque, José Pimentel, José Miguéns, Isidro Cortes-Ciriano, and João T. Barata

SUPPLEMENTAL INFORMATION

Supplementary Table 1. Summary of the clinical data of BMs patients and experimental results from PDX and PDC models.

Patient										PDX models								PDC
										Subcutaneous				Intracardiac				
Pt. No.	Sample ID	Gender	Age	Primary tumor	Location (ST/IT)	Specific location	No. of BMs	Previous Radiation (RT/RS)	Overall survival (months)	Engrafted	Latency time (days)	Metastases	CNS Metastases	Engrafted	Survival (Days)	Metastases	CNS Metastases	Yes/No
1	MET-CF29	F	70	Bladder	ST	Skull	1	No	7.4	Yes	31 (24-67)	No	No	Yes	45 (42-67)	Yes	Yes (B)	Yes
2	MET-CF30	M	72	Lung	IT	Cerebellar hemisphere	2	No	5.8	Yes	69 (58-76)	No	No	Yes	144 (130-158)	Yes	No	Yes
3	MET-CF32	M	80	Bladder	ST	Temporal	2	No	16.7	Yes	70	No	No	NP	-	-	-	No
4	MET-CF38	M	49	Lung	IT	Cerebellar hemisphere	1	No	10.4	Yes	20 (18-29)	Yes	No	NP	-	-	-	No
5	MET-CF58	M	65	Lung	ST	Parietal	2	No	7.4	Yes	22 (18-47)	Yes	No	NP	-	-	-	No
6	MET-CF63	F	44	Breast	ST	Fronto-parietal	2	No	10.1	No	-	-	-	-	-	-	-	No
7	MET-CF65	M	25	Osteosarcoma	ST	Frontal	1	No	2.5	Yes	20 (22-30)	No	No	Yes	64 (61-72)	Yes	No	Yes
8	MET-CF66	F	66	Lung	ST	Frontal	1	No	15	Yes	31 (24-35)	Yes	Yes (LM)	Yes	175	Yes	No	No
9	MET-CF67	M	54	Lung	IT	Cerebellar hemisphere	1	RS	20.3	No	-	-	-	-	-	-	-	No
10	MET-CF68	M	59	Lung	ST	Frontal	1	No	19.3	Yes	26 (24-35)	Yes	No	Yes	65 (63-141)	Yes	No	Yes
11	MET-CF69	M	76	Melanoma	ST	Frontal	3	No	1.2	Yes	33 (38-46)	Yes	No	Yes	70 (60-75)	Yes	Yes (B+LM)	Yes
12	MET-CF70	F	80	Colon	IT	Vermis	1	No	8.1	Yes	34 (28-39)	Yes	No	Yes	83 (80-95)	Yes	Yes (B+LM)	Yes
13	MET-CF71	F	41	Nasosinusal	ST	Skull	1	No	17.8	No	-	-	-	-	-	-		No
14	MET-CF73	M	60	Renal	ST	Occipital	1	No	16.9	No	-	-	-	-	-	-	-	No
15	MET-CF74	M	59	Renal	ST	Orbital	1	No	4.1	No	-	-	-	-	-	-	-	No
16	MET-CF75	F	58	Colon	IT	Cerebellar hemisphere	1	No	2.4	Yes	46 (46-183)	No	No	No	-	-	-	Yes
17	MET-CF76	F	62	Lung	ST	Frontal	3	RT	16.8	No	-	-	-	-	-	-	-	No
18	MET-CF78	M	61	Lung	IT	Cerebellar hemisphere	2	No	6.5	Yes	26 (21-37)	Yes	Yes (LM)	Yes	77 (61-88)	Yes	No	Yes
19	MET-CF79	F	64	Lung	ST	Occipital	1	RS	10.3	Yes	62 (58-74)	No	No	Yes	145 (11-289)	Yes	No	No
20	MET-CF80	M	64	Lung	IT	Vermis	1	No	3.5	Yes	61 (40-102)	Yes	No	NP	-	-	-	Yes
21	MET-CF81	F	67	Endometrium	IT	Cerebellar hemisphere	9	No	1.5	Yes	33 (29-44)	Yes	No	Yes	131 (76-163)	Yes	Yes (B)	Yes
22	MET-CF82	M	72	Colon	ST	Temporal	1	No	6.1	Yes	62 (47-74)	Yes	No	Yes	186 (72-199)	Yes	-	Yes
23	MET-CF83	F	68	Breast	IT	Vermis	1	No	11.7	No	-	-	-	-	-	-	-	No
24	MET-CF84	F	54	Breast	IT	Cerebellar hemisphere	2	No	6.3	No	-	Yes	No	-	-	-	-	No
25	MET-CF85	M	73	Lung	ST	Frontal	2	RS	11.4	No	-	Yes	No	-	-	-	-	No
26	MET-CF87	M	67	Lung	ST	Temporal	1	No	11.3	Yes	45 (43-100)	Yes	No	Yes	114 (10-144)	Yes	Yes (B)	Yes
27	MET-CF88	M	55	Prostate	ST	Frontal	2	No	4.9	Yes	92 (64-166)	No	No	No	-	-	-	Yes
28	MET-CF89	M	81	Colon	IT	Cerebellar hemisphere	3	No	4.9	Yes	26 (22-34)	No	No	Yes	83 (64-92)	Yes	Yes (B)	Yes
29	MET-CF90	M	68	Lung	IT	Vermis	1	No	1.1	Yes	78	Yes	Yes (LM)	NP	-	-	-	No
30	MET-CF92	M	73	Lung	ST	Temporal	1	No	9.6	Yes	120	No	No	NP	-	-	-	No
31	MET-CF93	M	63	Lung	IT	Cerebellar hemisphere	1	No	6.2	No	-	-	-	-	-	-	-	No
32	MET-CF94	M	47	Lung	ST	Frontal	2	RS	6.1	No	-	-	-	-	-	-	-	No
33	MET-CF95	M	65	Lung	ST	Temporal	2	No	4.9	No	-	-	-	-	-	-	-	No
34	MET-CF96	F	55	Breast	ST	Parietal	3	No	3.4	Yes	65 (58-72)	No	No	NP	-	-	-	No
35	MET-CF97	F	81	Colon	ST	Temporal	2	No	3.0	Yes	75	No	No	NP	-	-	-	No

PDX: Patient-derived xenograft; PDC: Patient-derived culture; ST: Supratentorial; IT: Infratentorial; RT: Radiotherapy; RS: Radiosurgery; CNS: Central nervous system; B: Brain; LM: Leptomeninges; NP: Not performed. All values are presented as median with interquartile range. Related to Figure 1.

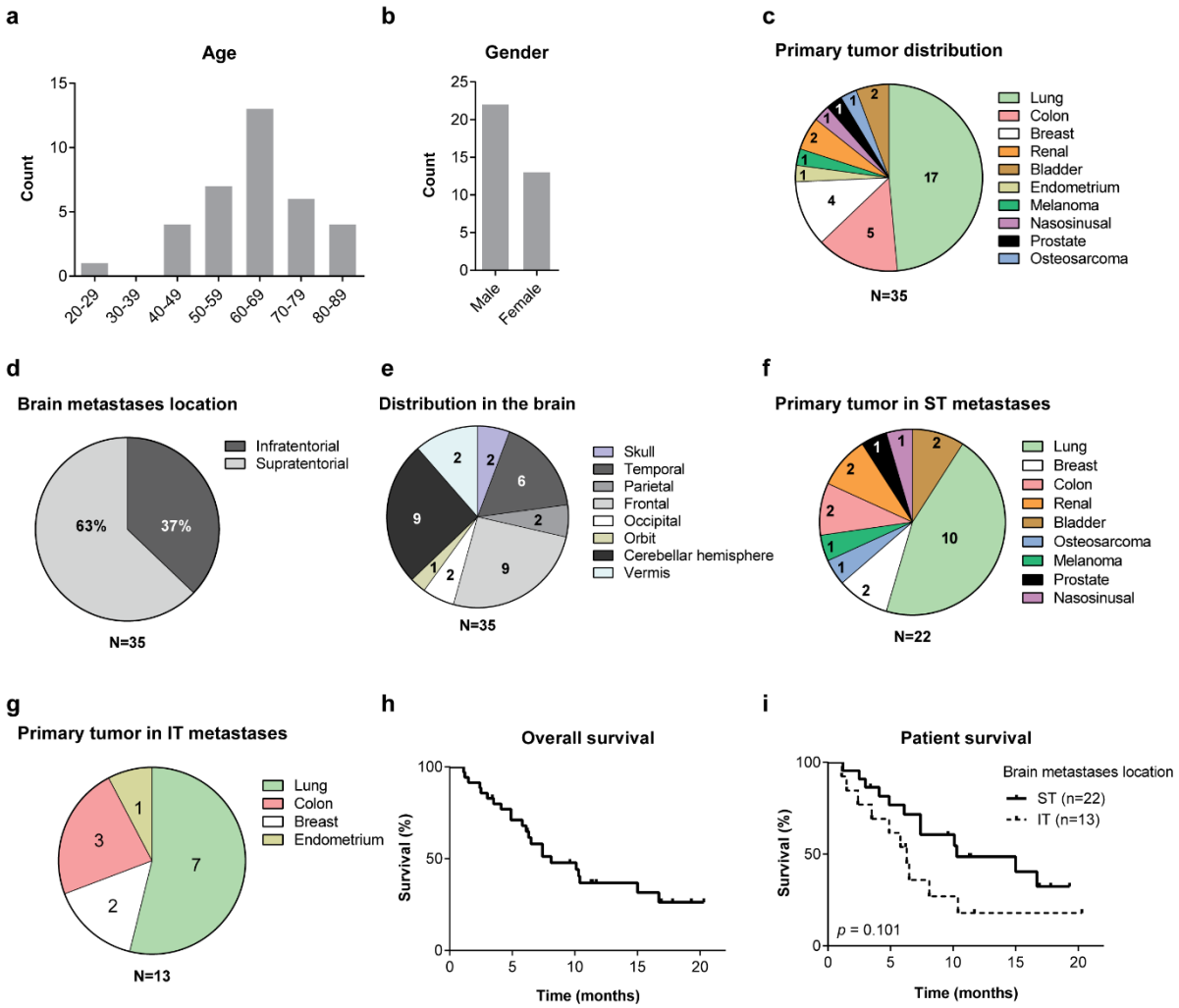

Supplementary Figure 1. Clinical characterization of the cohort of patients with BMs.
(**A**) Age of patients at the time of BMs surgery. (**B**) Gender distribution. (**C**) Distribution of patients according to the primary tumor. (**D**) Percentage of BMs in the supratentorial and infratentorial compartments. (**E**) Anatomical location of BMs. (**F-G**) Distribution of primary tumors according to the location in the intracranial compartments. (**H**) Overall survival of patients upon diagnosis of BMs. (**I**) Patient overall survival according to the metastases location in the intracranial compartments. ST: Supratentorial; IT: Infratentorial. Differences were considered statistically significant for p-values<0.05, according to the Log-rank (Mantel-Cox) test. Related to Figure 1.

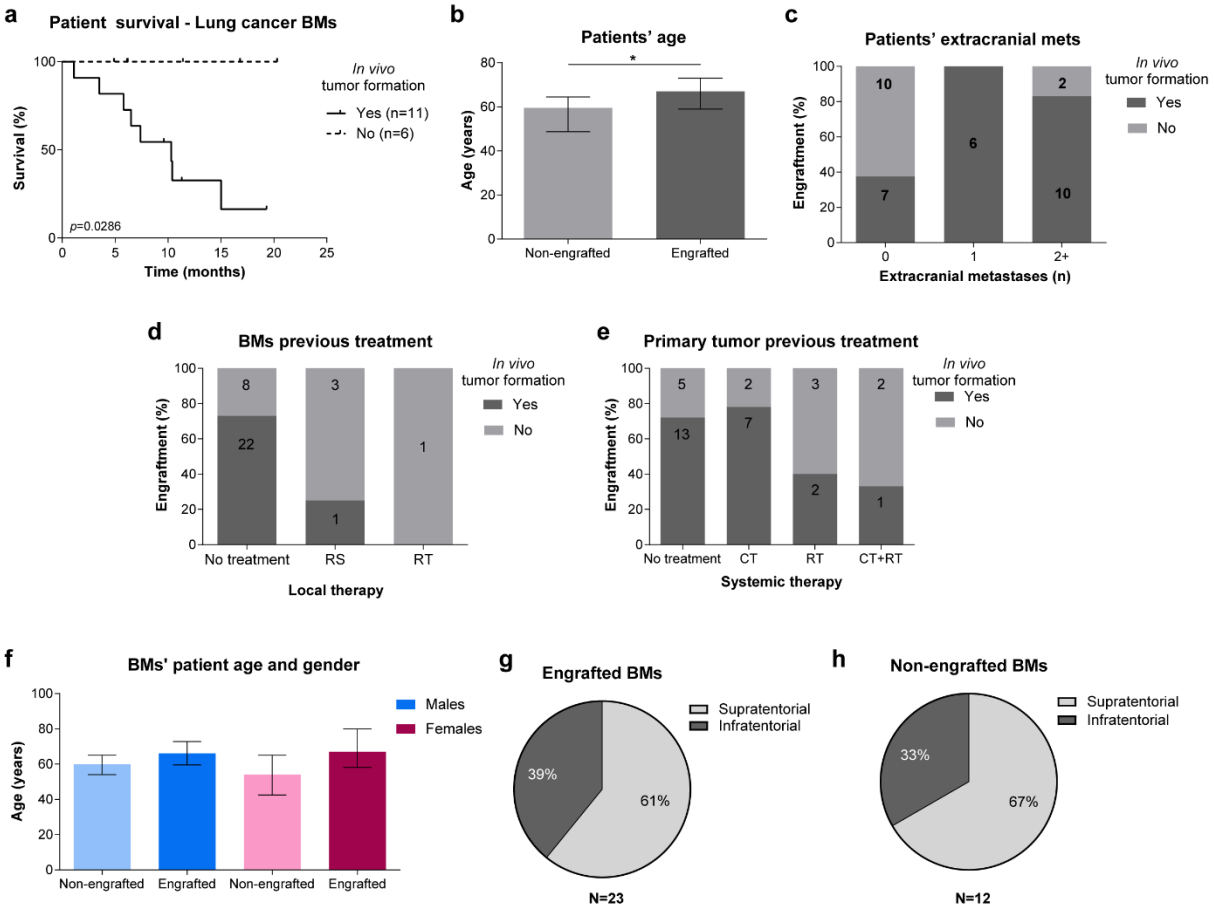

Supplementary Figure 2. Impact of clinical features on BMs engraftment.
(**A**) The *in vivo* tumorigenic potential of lung cancer BMs surgical samples correlates with patient poor survival (p=0.0286). (**B**) Engrafted samples derived from significantly older patients (p=0.0228). (**C**) Samples derived from patients displaying one or more extracranial metastases seem to have better engraftment ability. (**D**) BM local treatment seem to decrease engraft ability. (**E**) Treatment to the primary tumor with radiotherapy seems to decrease the ability of BMs to engraft in mice. (**F**) Comparison of patient median age for both engrafted vs non-engrafted samples by gender. (**G** and **H**) Distribution of BMs between supratentorial (ST) and infratentorial (IT) compartments for both engrafted and non-engrafted samples. Differences were considered statistically significant for p-values<0.05, according to an unpaired non-parametric Mann-Whitney test and to the Log-rank (Mantel-Cox) test. Related to Figure 1.

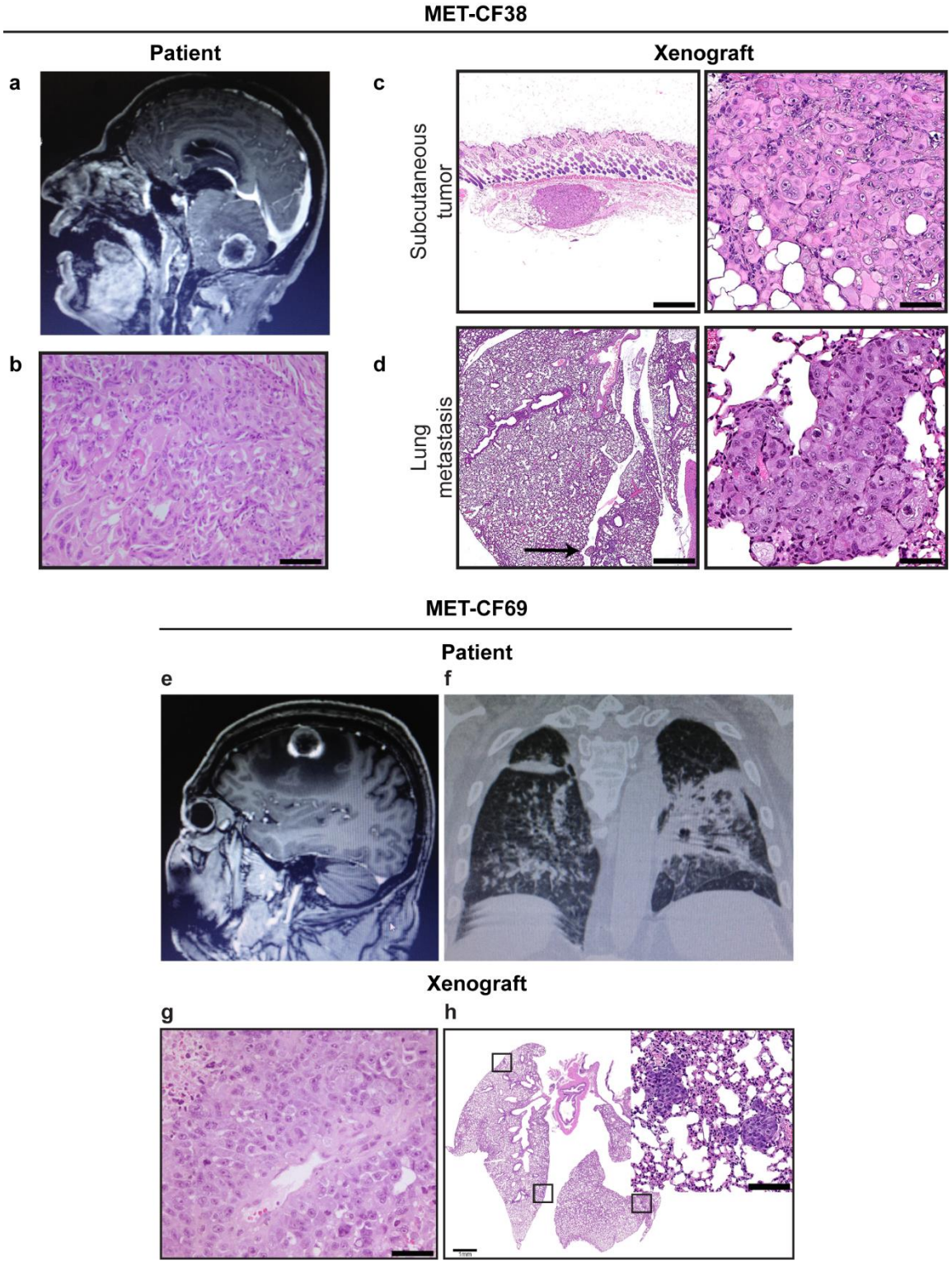

Supplementary Figure 3. Comparison of clinical cases and their matched subcutaneous PDXs models. Representative clinical case of a 49 years-old male patient with a stage IV lung adenocarcinoma where the BM (MET-CF38) xenografted in the mice flank originated spontaneous metastases in the lungs of the PDX. (**A**) Magnetic Resonance Imaging (MRI) of the brain, sagittal T1 contrast-enhanced sequence, showing a BM in the cerebellum. (**B**) H&E staining of the patient BM. (**C**) Corresponding H&E staining of the mouse flank xenograft. (**D**) Exclusive dissemination to the mouse lungs through passaging. Arrow indicates metastasis's location.
Representative clinical case of a 76 years-old male patient with metastatic melanoma to the brain (MET-CF69) and to the lungs, where the xenografted BM originated spontaneous metastases in the mice lungs. (**E**) Brain MRI, sagittal T1 contrast-enhanced, showing a left frontal BM. (**F**) Computed Tomography (CT) scan of the patient's lungs showing a diffuse infiltration by cancer cells. (**G**) H&E staining of the patient BM (20x). (**H**) H&E staining of the mice lungs exhibiting multiple metastases (squares). Scale bars: (B) 50µm, (C) 1mm and 50µm, (D) 1mm and 50µm, (G) 50µm, (H) 1mm. Related to Figure 2.

Supplementary Table 2. Matched patient and mice metastatic sites in subcutaneous PDX models.

Primary tumor	Sample ID	Metastases location									
		CNS	Lungs	Liver	Spleen	Kidney	Intraperit.	Lymph nodes	Soft tissues	Gonads	Bone/ Bone marrow
Lung	MET-CF38										
	MET-CF58										
	MET-CF66										
	MET-CF68										
	MET-CF78										
	MET-CF80										
	MET-CF85										
	MET-CF87										
	MET-CF90										
Melanoma	MET-CF69										
Colon	MET-CF70										
	MET-CF82										
Endometrium	MET-CF81										
Breast	MET-CF84										

Red - organs with tumor involvement in the patient; Green - organs with tumor involvement in the mouse; Yellow - organs with tumor involvement in both patient and mouse. Related to Figure 2.

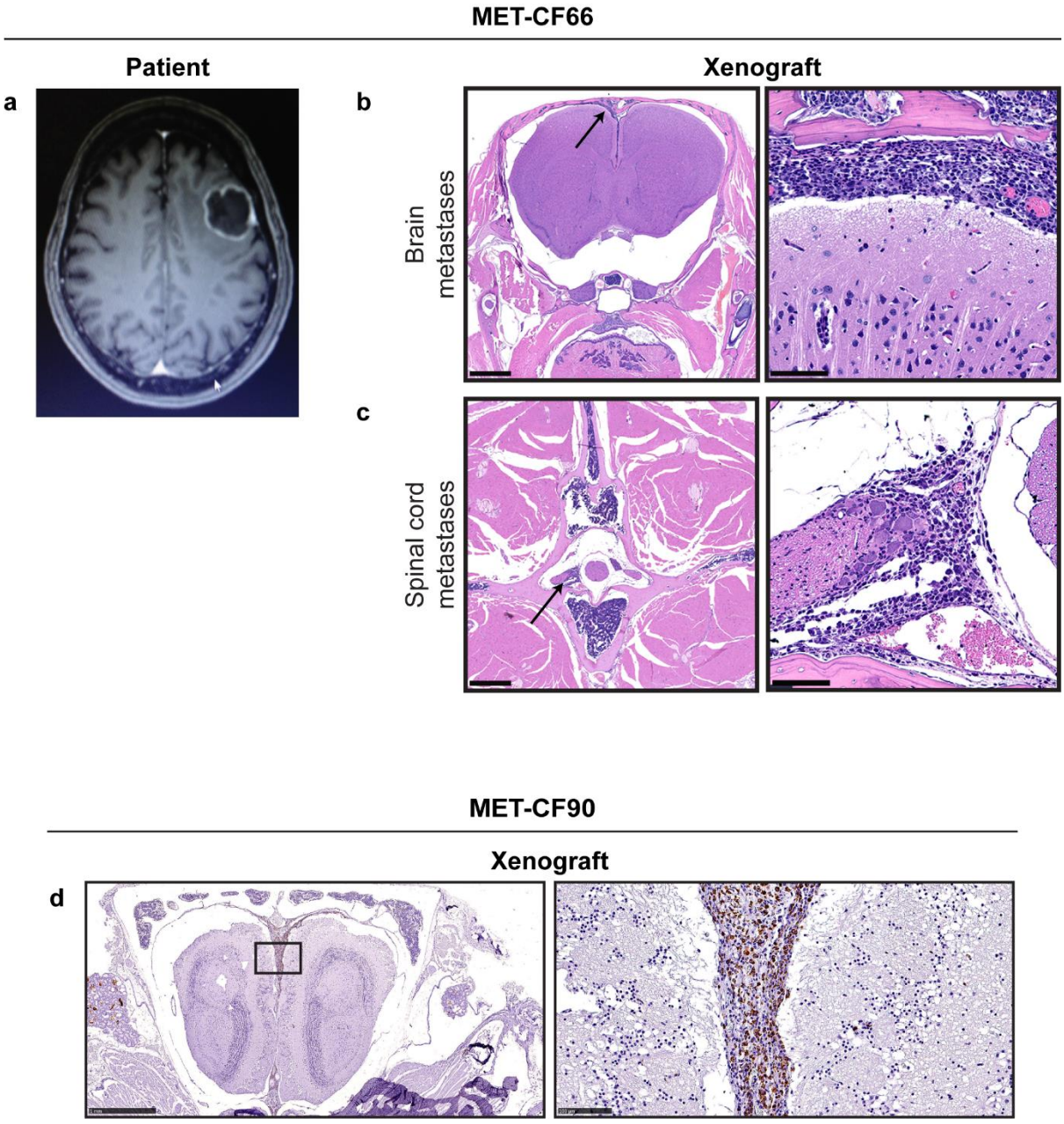

Supplementary Figure 4. Spontaneous CNS leptomeningeal dissemination in flank implanted BMs from lung cancer.
(**A**) Brain MRI, axial T1 contrast-enhanced sequence, of a 66 years-old female patient with a left frontal BM from lung adenocarcinoma (MET-CF66). (**B-C**) H&E staining showing spontaneous leptomeningeal dissemination to the brain and the spinal cord in the matched mouse xenograft. Arrow indicates metastasis's location. (**D**) Representative anti-human mitochondria staining of a mouse brain with leptomeningeal dissemination derived from a 68 years-old patient with a posterior fossa BM from lung adenocarcinoma (MET-CF90). Scale bars: (B) 1mm and 100µm, (C) 1mm and 100µm, (D) 1mm and 100µm. Related to Figure 2.

Supplementary Table 3. Matched patient and mice metastatic sites in intracardiac PDX models.

Primary tumor	Sample ID	Metastases location												
		CNS	Lungs	Liver	Kidney	Suprarenal	Intraperit.	Spleen	Gonads	Orbita	Mandibula	Soft tissues	Bone/Bone marrow	Subcut.
Lung	MET-CF30													
	MET-CF66													
	MET-CF68													
	MET-CF78													
	MET-CF79													
	MET-CF87													
Osteosarcoma	MET-CF65													
Melanoma	MET-CF69													
Colon	MET-CF70													
	MET-CF82													
	MET-CF89													
Bladder	MET-CF29													
Endometrium	MET-CF81													

Red - organs with tumor involvement in the patient; Green - organs with tumor involvement in the mouse; Yellow - organs with tumor involvement in both patient and mouse. Related to Figure 4.

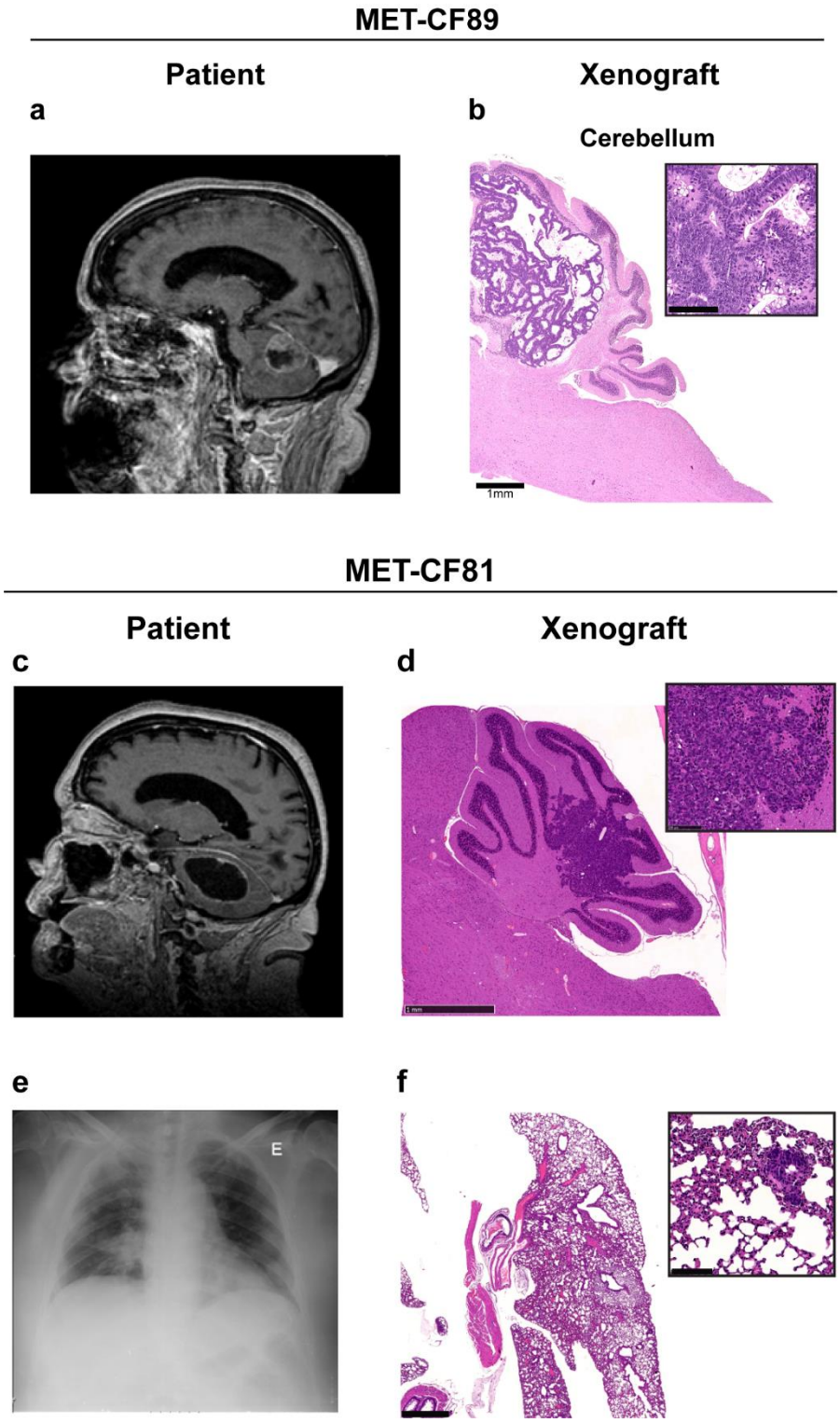

Supplementary Figure 5. Comparison of clinical cases and their matched intracardiac PDXs models. Intracardiac xenograft of a surgically resected cerebellar BM (MET-CF89) from a patient with colon cancer mirrored the intracranial location of the patient's tumor. (**A**) Brain MRI, sagittal T1 contrast-enhanced sequence, of an 81 years-old male patient with a BM in the cerebellum from a colon carcinoma. (**B**) Corresponding H&E staining of a metastasis in the mouse cerebellum.
Representative clinical case of a 67 years-old female patient with metastatic endometrium cancer derived BM (MET-CF81), where the intracardiac xenograft shared two metastatic sites with the donor. (**C**) Brain MRI, sagittal T1 contrast-enhanced sequence, showing a cystic BM in the cerebellum and (**D**) the correspondent H&E staining of the mouse metastasis in the cerebellum. (**E**) Right lung metastases in the patients' chest X Ray and (**F**) the matched lung metastases in the xenograft. Scale bars: (B) 1mm and 100µm, (D) 1mm and 100µm, (F) 1mm and 100µm. Related to Figure 4.

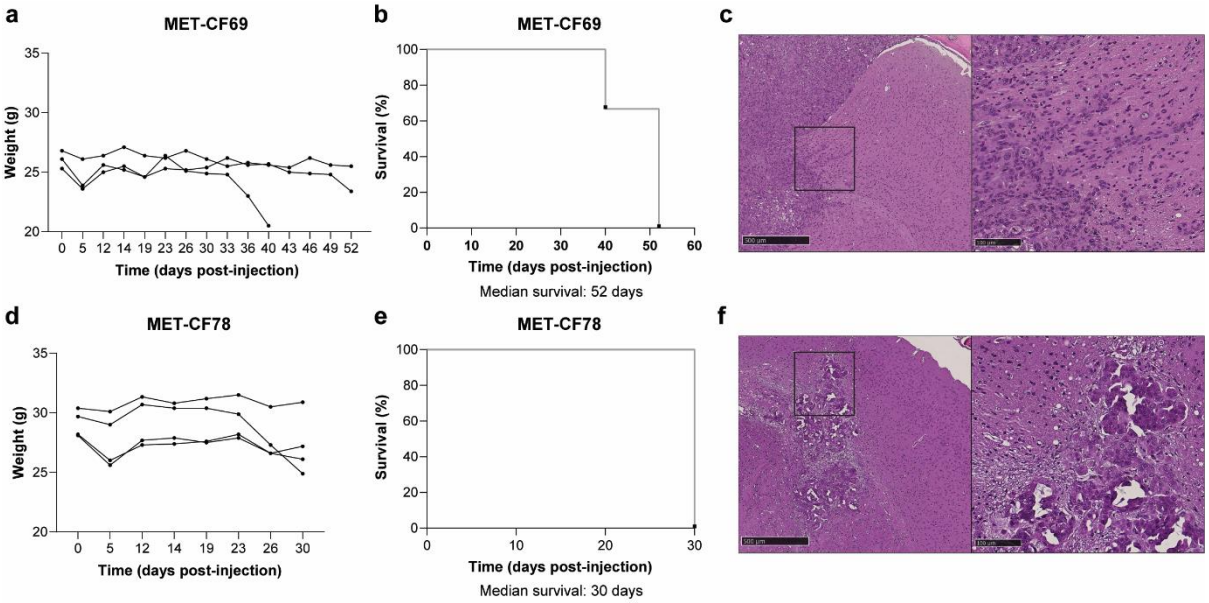

g

PDC	Primary tumor	Histological evaluation				
		Brain invasion	Brain dissemination	Brain stem/cerebellum dissemination	Spinal cord thoracic dissemination	Spinal cord lumbar dissemination
MET-CF69 (N=3)	Melanoma	3/3 (3/3 HI)	0/3	0/3	0/3	0/3
MET-CF78 (N=4)	Lung	4/4 (2/4 HI)	3/4	2/4	2/4	2/4

Supplementary Figure 6. *In vivo* models of orthotopic implanted BMs.
PDCs were established from subcutaneous xenografts of BM samples derived from patients with (**A-C**) a melanoma and (**D-F**) a lung carcinoma. The growth pattern of these PDCs in the brain was assessed after intracranial injection of cells in mice. (**A** and **D**) Body weight variation throughout time, (**B** and **E**) survival curves and (**C** and **F**) H&E sections of brain tumors are shown for each PDC in 5x (left) and 20x (right) amplifications. (**G**) Histological evaluation of H&E sections of mice CNS was performed to evaluate the pattern of brain invasion and dissemination, as well as the dissemination along the spinal cord. Scale bars: (C) 500µm and 100µm, (F) 500µm and 100µm. Related to Figure 6.

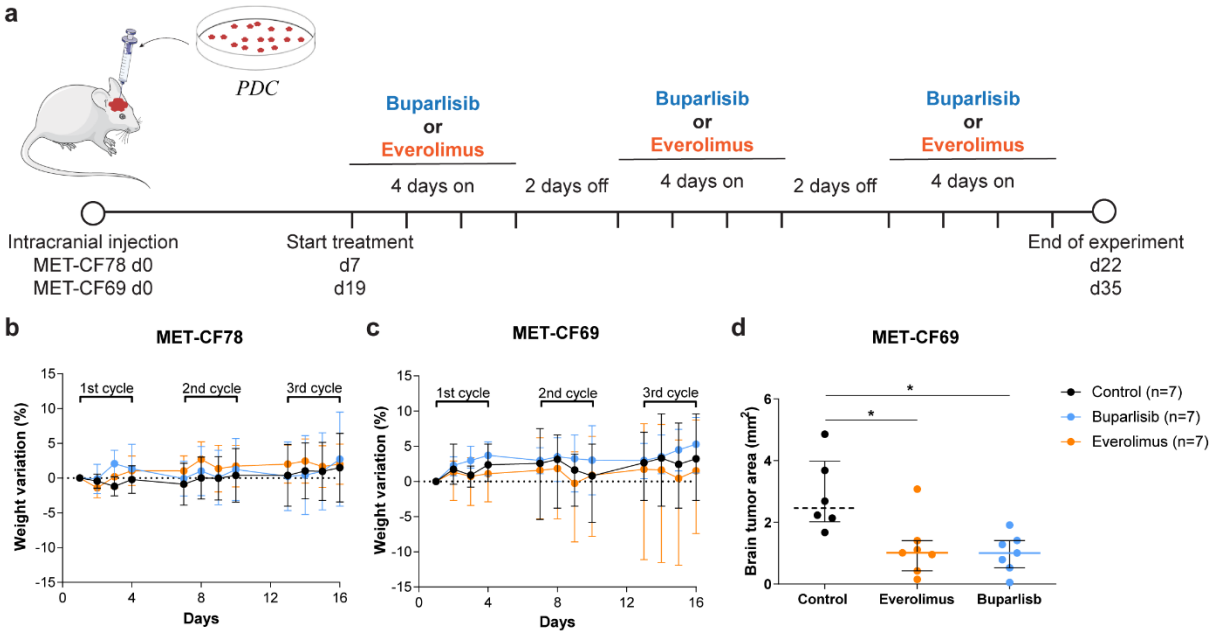

Supplementary Figure 7. Patient-derived xenografts were established by the intracranial injection of PDCs to assess the efficacy of buparlisib and everolimus in vivo.
(**A**) Representative scheme of the treatment evaluation performed in xenografts established by the intracranial injection of PDCs derived from BM samples of a lung (MET-CF78) and a melanoma (MET-CF69) cancer patients. Animals were randomly divided in 3 groups: buparlisib (30mg/kg/day; n=7), everolimus (3mg/kg/day; n=7), and vehicle (5% DMSO/30% PEG300/H_2O; n=7) used as a negative control for comparison. Treatment administration was performed in 3 cycles of therapy with buparlisib and everolimus. Body weight variation was assessed throughout time for (**B**) MET-CF78 and for (**C**) MET-CF69. (**D**) Histological sections of the CNS were evaluated to assess the tumor area in the brain. Data is represented as median with interquartile range. Differences were considered statistically significant for p-values<0.05, according to the Mann-Whitney test. Related to Figure 6.